Influence of Cations on Direct CO_2 Capture and Mineral Film Formation: the Role of KCl and $MgCl_2$ at Air/Electrolyte/Iron Interface

Chathura de Alwis[1], Kayleigh Wahr[2], Kathryn A. Perrine*

Department of Chemistry, Michigan Technological University, Houghton, MI 49931

*Corresponding author

Abstract

Uncovering the mechanisms associated with CO_2 capture through mineralization are vital for addressing rising CO_2 levels. Iron in planetary soils, the mineral cycle, and atmospheric dust, react with CO_2 through complex surface chemistry. Here, the effect of cations on the growth of carbonate films on iron surfaces was investigated. *In situ* polarized modulated infrared reflection absorption spectroscopy was used to measure CO_2 adsorption and oxidation of iron in $MgCl_2(aq)$ and KCl(aq), compared to $FeCl_2(aq)$ at the air/electrolyte/iron interface. The cation was found to influence the film composition and growth rates, corroborated by infrared and photoelectron spectroscopy. In $MgCl_2(aq)$ a mixture of hydromagnesite, magnesite, and a Mg hydroxy carbonate film was grown on iron, while in KCl(aq) a potassium rich bicarbonate film was grown. The cations were found to affect the rates of hydroxylation and carbonation confirming a specific cation effect on carbonate film growth. In the submerged region, a heterogeneous mixture of lepidocrocite and iron hydroxy carbonate was produced suggesting that Fe^{2+} dominates the surface products. Surface roughness measurements from *in situ* atomic force microscopy indicate iron initially corrodes faster in $MgCl_2(aq)$ than KCl(aq), due to the Cl^- ions that initiate pitting and corrosion. In this region, cations were not found to affect the morphologies. This study shows surface corrosion is necessary to provide nucleation sites for film growth and that the cations influence the carbonate film, relevant for CO_2 capture and planetary processes.

Keywords: carbon capture, minerals, electrolyte/solid interface, redox reactions, surface carbonation, *in situ* spectroscopy, cations

Abbreviations: X-ray photoelectron spectroscopy (XPS), polarized modulated-infrared reflection absorption spectroscopy (PM-IRRAS), attenuated total reflectance-Fourier transformed infrared (ATR-FTIR), atomic force microscopy (AFM)

1.0 Introduction

CO_2 levels rose over 400 ppb over several decades[1], which are causing drastic effects in weather patterns, melting of ice-caps, ocean acidification, and atmospheric corrosion.[2] [3] [4] These global issues have severe impacts on populations, limiting water resources, and contribute to rising sea levels. The presence of high levels of CO_2 calls for atmospheric removal through capture methods by either geochemical storage through sequestration or by conversion of CO_2 to other commodity chemicals in the fuel industry. [2] [5] [6] [7]

One way to mitigate rising CO_2 levels is through capture and subsequent mineralization, converting adsorbed CO_2 into carbonates from industrial waste, mine tailings, or cement by storing it underground.[8] Direct air capture involves solvent or solid-based absorbents, where solutions, brines, and oxides have high capacities for CO_2 absorption. Challenges in the mineralization process, include absorptivity of the materials, precipitation of products, and surface passivation, fundamentally involve surface chemistry at air/solution/metal interfaces. Understanding the mechanisms of CO_2 adsorption on earth-abundant materials in solutions could be used to alter the binding of CO_2 that may provide new routes for increasing carbonation rates.

These same mechanisms are also important for interpreting other complex interfaces in geological formation and environmental processes on Earth and extraterrestrial planets.[9, 10] Iron is an earth-abundant material that is prevalent in Earth's mineral cycle as atmospheric dust[11] [12] [13] and soils[14], that comprise minerals on Venus and Mars.[15] Uncovering mechanisms associated with mineral carbonation may reveal how these planets evolved.[16, 17] Iron surface chemistry also plays a vital role in film formation (known as inorganic scale) on water pipelines.[18] [19] [20] [21] [22] [16] In these environments, where complex interfaces are present, iron surfaces are known to undergo reduction-oxidation reactions resulting in dissolution. Redox reactions are further accelerated with exposure to aqueous mixtures of dissolved ions and organics as well as reactive atmospheric gases, such as CO_2 and O_2.

Converting CO_2 into carbonate is the core reaction step for mineralization and essential to understanding kinetics of carbon capture. In solution and at liquid/solid interfaces, ultra-thin layers of water are cited as necessary providing ion solvation and diffusion for CO_2 transportation.[23] It is proposed this leads to ion-carbonate complexation, nucleation, and ultimately growth into carbonate films. Direct conversion of CO_2 into carbonate minerals is thought to occur through the dissolution of CO_2 to form carbonic acid and then either proton neutralization or by reaction with cations to form carbonates. These steps depends on variations in pH, the cation, and temperature.[24] The details of these steps are still not well understood, but critical to understanding mineral carbonation.

On solid interfaces, metal oxide surfaces have been shown to have a high absorption capacity for CO_2. Magnesium oxide (MgO) and calcium oxide (CaO), present in various water sources[25], are the preferred materials for CO_2 capture, due to the high absorption rate of Mg^{2+} and Ca^{2+}.[26] [27] [28] [29] Other studies have shown that metal hydroxides ($Fe(OH)_2$, $Co(OH)_2$, $Ni(OH)_2$) are efficient adsorbents for capturing CO_2, producing metal carbonate (MCO_3) and H_2O as products.[30] Correlations have been found between CO_2 uptake and humidity, where water dissociation provides basic OH sites for reaction with the acidic CO_2.[27] [31] [32] Studies have shown oxide supports modified with other alkali metals have a high capacity for CO_2 adsorption.[27] These reactions involve both the air/liquid and liquid/solid interfaces, where tailoring the properties of solutions and materials surfaces have the potential for efficient, direct CO_2 capture.[2] [27]

Our group has developed an *in situ* method for investigating these complex interfaces using polarized modulated infrared reflection absorption spectroscopy (PM-IRRAS), where both the air/liquid and liquid/solid interfaces are measured simultaneously.[33-35] This technique allows for tracking the vibrational signatures of complex interfaces, where atmospheric gases (CO_2 and O_2) adsorb at the air/liquid/solid interface thus initiating surface oxidation. In our previous studies we have used PM-IRRAS to measure surface oxidation of iron in NaCl(aq) and $CaCl_2$(aq) electrolytes, which produce interfacial mineral carbonate films.[33, 35] It was found that Na^+ ions from NaCl(aq) serve as a spectator ion producing $FeCO_3$ (siderite). For iron in $CaCl_2$(aq), Ca^{2+} ions were found to effect the growth of a $CaCO_3$ film at air/$CaCl_2$(aq)/Fe interface.[33] In addition, the concentration of Cl^- ions in the solution was found to effect on the rate of corrosion, influencing the film growth.

In this study, we aimed to measure how other alkali and alkaline cations affect surface corrosion, CO_2 capture, and the interfacial mineralization at the air/solution/Fe interface. The objectives were to: 1) measure the rates of carbonation from CO_2 adsorption on film growth, 2) characterize the mineral films and the effect of the cations, and 3) connect film growth with surface corrosion. *In situ* PM-IRRAS was used to measure the vibrational signatures of interfacial iron oxidation in $MgCl_2$(aq) or KCl(aq) at the air/electrolyte/Fe interface to test whether other cations will directly adsorb CO_2. Here, effect of Mg^{2+} and K^+ ions on the mineral film formation and composition was measured. The film composition is confirmed by *ex situ* attenuated total reflectance Fourier transform infrared (ATR-FTIR) spectroscopy and X-ray photoelectron spectroscopy (XPS) analysis. The results are compared with iron oxidation in $FeCl_2$(aq) to test the competition of the cations with Fe^{2+} on the mechanism of film formation. The physical changes of the Fe surface were measured using *in situ* atomic force microscopy (AFM) to find the apparent rate of corrosion and the connection with film growth and surface morphology. These findings address complex interfacial chemistry in the natural environment, including geochemical processes, catalytic reactions of CO_2 capture, and corrosion contributing to material degradation.

2.0 Methods

2.1 Sample preparation

Two grades of metallic iron samples were used for the experiments. Metal plates of high purity iron (Puratronic, 99.995% metals basis, Alfa Aesar) and low purity metal Fe (iron(II), 99.99%, Allied Metals Corp.) were obtained and cut into small pieces (2.0 cm × 1.0 cm × 0.20 cm) using a mechanical saw. One side of each sample was polished to a mirror finish. First, the samples were mounted in plastic molds of blue diallyl phthalate by applying 5 bar pressure for 15 minutes at 220 ºC in a mounting press. Then one side of each sample was polished using sandpaper with different grit sizes (400, 600, 800, and 1200) using a metal polishing instrument (Struers, LaboPol-1). The last polishing step was completed by polishing with 0.05 μm silica suspension on a polishing pad (Allied High Tech Pan B). The polished samples were cleaned using a three-step procedure that has been described previously.[34 35] The surface polishing gives a reflective surface required for the PM-IRRAS experiments and also for obtaining a surface with a low number of defects. The samples were washed using Micrell soap and rinsed with nanopure water (18.2 MΩ cm, Millipore Inc.). Lastly, they were sonicated in ethanol for 15 minutes to dry the samples, prior to PM-IRRAS and AFM experiments.

Solution preparation: A 100 mM KCl(aq) stock solution (KCl 99.999%, trace metal basis, Thermo Scientific), a 100 mM $MgCl_2$(aq) stock solution ($MgCl_2$ 99.99%, trace metal basis, Sigma-

Aldrich), and a 50 mM $FeCl_2$(aq) stock solution ($FeCl_2$ $4H_2O$, puriss, p.a. >99.0%, Sigma-Aldrich) were prepared using nanopure water (18.2 MΩ cm, Millipore Inc.). The interfacial PM-IRRAS experiments were carried out with 10 mM concentrations of KCl(aq), $MgCl_2$(aq), or $FeCl_2$(aq) by diluting the stock solutions in a 50 mL beaker, which was used as part of the liquid cell. Solutions of 1 mM concentrations were used for *in situ* AFM corrosion experiments where the stock solutions of KCl(aq) and $MgCl_2$(aq) were prepared using serial dilution. For the drop and dry experiment, a 10 mM $KHCO_3$ solution was prepared.

2.2 PM-IRRAS measurements at the air/electrolyte/iron interface

An iS50R Fourier transform infrared spectrometer (ThermoScientific, Inc.) instrument coupled with custom-built liquid cell[34] was used to collect PM-IRRAS infrared reflectance absorbance spectra of the samples at the air/electrolyte/iron interface. An Al coated flat mirror and a parabolic mirror were used to focus the IR beam on the iron sample, at a grazing angle of 76 degrees. A photoelastic modulator (PEM, Hinds, Inc.), equipped with a ZnSe window and polarizer, was used to modulate the signal between the p and s polarization. The polished Fe sample was oriented vertically by attaching it to the sample holder via an alligator clip. The incident infrared signal is focused onto the center of the polished surface and reflected at an angle of 76 degrees, as shown in Figure 1A-B. This high grazing angle gives PM-IRRAS a high surface sensitivity, with a penetration depth of ≈ 0.4 μm (for iron) and up to 1.2 μm (for iron oxide).[35] The half wave of the Bessel function was set to 2100 cm^{-1} to collect PM-IRRAS at air/electrolyte/iron interfaces. All PM-IRRAS spectra were collected within a 4000 – 600 cm^{-1} spectral range, a gain of 8.0, a 4.0 cm^{-1} resolution, an aperture of 5%, and 1000 scans per spectrum.

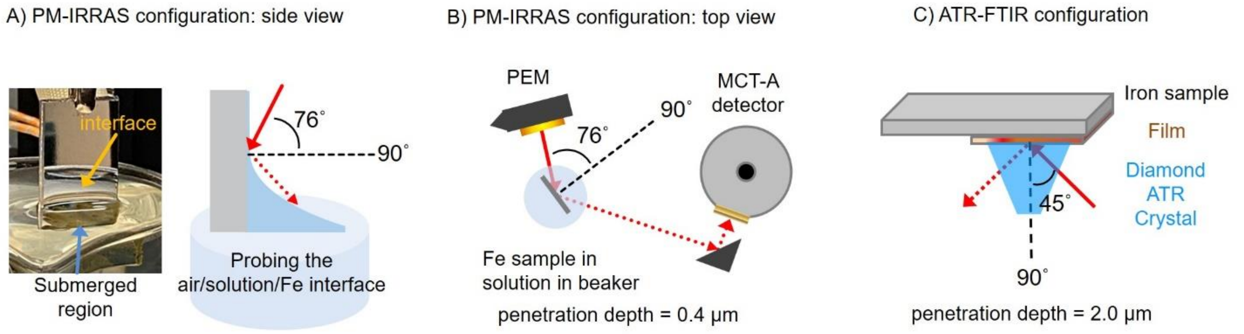

Figure 1: Reflectance geometry of the vibrational spectroscopy measurements in A-B) the PM-IRRAS reflectance mode, using an angle of reflection of 76 degrees, and C) the diamond ATR crystal using a fixed angle of 45 degrees. PM-IRRAS probes the air/solution/Fe interface while ATR-FTIR spectroscopy measures both the interface and submerged regions after surface oxidation.

The optical alignment of the light source onto the iron surface and the optimization of the peak to peak (p/p) interferogram signal were done, as described previously.[34] Five PM-IRRAS spectra were collected in each stage of the experiment with either 10 mM KCl(aq), 10 mM $MgCl_2$(aq), or 10mM $FeCl_2$(aq) electrolytes. First, a few spectra of the cleaned, polished iron surface were collected before exposure to the solutions to ensure that the sample was free of any impurities. Next, an empty 50 mL beaker was placed under the iron sample, where a few PM-IRRAS spectra were collected of the dry iron surface that were used for baseline corrections. The beaker was then filled with nanopure water (18.2 MΩ cm, Millipore Inc.) until the p/p signal of the interferogram was reduced by half to ensure that the water attenuated the p/p signal, indicating that the PM-IRRAS signal was probing the iron surface through the liquid film. Six spectra were collected in the nanopure water.

For stage 1, several (5-6) PM-IRRAS spectra of the air/electrolyte/Fe interface were recorded for an hour to observe any changes due to diffusion of the ions to the surface. In stage 2, 250 µL aliquots of the electrolyte solutions were removed so that the Fe interface was gradually exposed to air. This stage allowed for adsorption of atmospheric O_2 and CO_2 to the electrolyte/iron interface, initiating surface oxidation and corrosion. Spectra were collected after each aliquot over time to track the changes in the surface oxidation. This stage was continued until the p/p signal had returned close to its original value or until the p/p value did not change (no liquid layer was left on the surface). In the final 3rd stage, the iron surface was no longer in contact with electrolyte, allowing the surface to completely oxidize in air from exposure to atmospheric O_2 and CO_2. The collection of PM-IRRAS spectra continued in this (air oxidation) stage until no new peaks were observed in the spectra. The experiments were repeated 3-4 times per electrolyte to ensure reproducibility.

PM-IRRAS peak area fitting procedure

The baseline was corrected by subtracting the Bessel function baseline of the dry, polished Fe surface from each of the PM-IRRAS spectra collected in stage 1 (in solution), stage 2 (air adsorption), and stage 3 (air oxidation). Example raw spectra are shown in the supporting information in Figure S1. Quantitative analysis of the data was achieved by fitting the peak areas of the δOH and νCO_3 vibrational modes in the uncorrected PM-IRRAS spectra using the CasaXPS software. Each peak of the PM-IRRAS spectra was fitted with 100% Gaussian lineshape accompanied with a linear background. The total peak areas of the δOH and νCO_3 vibrational modes were normalized to the respective maximum peak area in stage 3 to find the relative coverage for each mode. These coverages were plotted as a function of time for stages 1 and 2 to obtain a rate of formation of hydroxylation and carbonation during the film growth.

2.3 Attenuated Total Reflectance-Fourier Transform Infrared (ATR-FTIR) spectroscopy

The same iS50R Fourier transform infrared spectrometer was used to collect ATR-FTIR spectra of the samples from the PM-IRRAS experiments using an DLaTGS detector. Three areas on the Fe sample were analyzed (shown in Figure 1A): 1) the polished (clean) iron surface that was not exposed to the electrolyte, 2) the interfacial region that was exposed gradually to both the electrolyte and atmospheric O_2 and CO_2, and 3) the region completely submerged in the electrolyte. The samples were directly analyzed without rinsing after drying in air for 120-240 minutes. All spectra were collected as a single beam spectrum using a gain of 4.0, 256 scans, a resolution of 4.0 cm^{-1}, and within the 4000 – 400 cm^{-1} spectral range. This probes the surface at a 45 degree angle with a probe depth of 2.0 µm, as shown in Figure 1C. Spectra of the interface and submerged regions were referenced to the single beam spectrum of the polished (clean) iron surface to produce absorbance spectra.

Absorbance spectra of natural mineral specimens comprised of Mg and K carbonates were used as references to compare with the infrared spectra. ATR-FTIR spectra of a goethite (α-FeOOH), lepidocrocite (γ-FeOOH), magnesite ($MgCO_3$), hydromagnesite ($Mg_5(CO_3)_4.(OH)_2.4H_2O$), artinite ($Mg_2(CO_3)(OH)_2{\cdot}3H_2O$), Pokrovskite ($Mg_2(CO_3)OH_2{\cdot}0.5H_2O$), nesquehonite ($Mg(HCO_3)OH·2H_2O$), Brugnatellite ($Mg_6Fe^{3+}(CO_3)(OH)_{13}·4H_2O$), coalingite ($Mg_{10}Fe^{3+}_2(OH)_{24}(CO_3)·2H_2O$), and Erythrosiderite ($K_2[FeCl_5(H_2O)]$,) were collected using the same spectral parameters but using the bare diamond window as the background spectrum. Specimen locale and spectra are given in the supporting information, in Figure S3. Mineral specimens were loaned from the A. E. Seaman Mineral Museum at Michigan Technological University, the Carnegie Museum of Natural History, and the Mineralogical & Geological Museum at Harvard University. Other standards of K_2CO_3 (99%, Sigma Aldrich) and MgO (98%, Acron) powders were collected, also using the bare diamond window as the background.

2.4 X-ray Photoelectron Spectroscopy (XPS)

A PHI 5800 XPS instrument (Perkin Elmer, Physical Electronics model) was used to collect survey spectra and high resolution XPS spectra. The base pressure of the XPS instrument is maintained at ultra-high vacuum ($1x10^{-9}$ Torr) pressure range. A Mg anode (1253.6 eV) at 15 kV operating voltage was used to scan the surface of the iron samples used in the PM-IRRAS and AFM experiments before and after oxidation. The analysis diameter of the X-ray beam on the sample was 800 µm and the angle between the sample and the analyzer was maintained at 45°, where the angle between the anode and the analyzer was 54.6°. Survey spectra were collected using a pass energy of 187.85 eV, step voltage of 0.8 eV, and a dwell time of 20 ms/step. High resolution spectra were collected using a pass energy of 23.50 eV, step voltage of 0.1 eV, and a dwell time of 100 ms/step for the C 1s, O 1s, K 2p, Fe 2p, Mg 1s, Mg 2p, and Cl 2p regions. XPS spectra of the three regions (polished, interface and submerged) were collected for samples obtained from PM-IRRAS experiments and from liquid AFM experiments. Two regions were collected from the samples analyzed using AFM: the center of the dried droplet submerged in solution and the interface region.

The CasaXPS software was used to fit all the high resolution XPS spectral peaks using a Shirley background and a 100% Gaussian lineshape. All regions were charge corrected with respect to the aliphatic carbon at 284.6 eV. Sensitivity factors were used to correct the peak areas for each region, when computing the elemental ratios.[36, 37]

2.5 Atomic Force Microscopy (AFM)

Atomic force microscopy was used to image the changes in the surface topography both in solution using *in situ* liquid AFM and after exposure to atmospheric O_2 and CO_2 in air (*ex situ)*. To investigate the initial stages of corrosion, high purity iron samples (99.995% iron) were exposed to 1 mM solutions of either $MgCl_2(aq)$ or KCl(aq). The solutions were prepared by diluting 50 mM concentrated solutions to the desired concentration using nanopure water. An Asylum MFP-3D atomic force microscope instrument was used to collect all images in the experiments.

***In situ* liquid AFM**: The iron surfaces were imaged in solution to observe the surface corrosion over time. Polished Fe samples were mounted onto glass microscope slides using carbon tape and placed on the instrument stage. Silicon probes coated with chromium and gold (Oxford Instruments OLTESPA with an Cr/Au reflective coating) with a frequency of 70 kHz and a force constant of 2 N/m were used to image samples in the 1 mM KCl(aq) or 1 mM $MgCl_2(aq)$ solutions. Similar silicon probes (Oxford Instruments with Al reflective coating) of the same frequency and force constants were also used for iron samples exposed to the electrolyte solutions. Images of the clean, polished iron surface were first collected in air to check the surface roughness prior to exposure of the electrolytes. Next, the electrolyte solution was added to the center of the iron sample using a micropipette to create a ~ 50 µL droplet. Care was taken for the droplet to not touch the edges of the sample, which would quickly initiate the corrosion. The head was used to lower the cantilever into the droplet and the surface was imaged using tapping mode (AC mode) at a scan rate of 0.60 Hz using 256 points per line. Images of areas 10 µm x 10 µm and 5 µm x 5 µm were collected in the same regions consecutively over a two-hour time period to track the surface roughness and morphology changes. Surface roughness was measured using the root mean squared (RMS) measurements of 1 µm x 1 µm size over several areas in the 5 µm x 5 µm images. Averages and standard deviations were obtained for at least 5 different areas. These surface roughness measurements were plotted as a function of time to obtain the apparent rate of corrosion. These rates in the electrolytes rates were compared to those in nanopure water, without influence of ions.

***Ex situ* AFM:** After the *in situ* imaging, the sample was rinsed using nanopure water and dried in air for 1+ hrs. During this time, atmospheric O_2 and CO_2 oxidized the sample. The surface was then re-imaged at various locations to observe the morphology changes of the surface. Images were collected with the Al-coated silicon tips using scan rates between 0.50-0.70 Hz, 256 points per line, in different areas of 10 µm x 10 µm, 5 µm x 5 µm, and 2.5 µm x 2.5 µm. All AFM images were processed using a 3rd order flattening. The samples from the PM-IRRAS measurements were also imaged without rinsing after air oxidation (stage 3) several days later, using scan rates between 0.5-1 Hz. Regions assessed were the interface region, the region below the interface, the submerged region, and the polished region.

3.0 Results and Discussion

3.1 CO_2 adsorption and oxidation at the air/electrolyte/iron interface

In order to detect the CO_2 adsorption, *in situ* PM-IRRAS was used with our 3-stage method to measure the vibrational signatures at the air/solution/Fe interface.[33] In stage 1, the iron surface is exposed to 10 mM of $MgCl_2(aq)$, $KCl(aq)$, or $FeCl_2(aq)$, where reflectance spectra is collected at the air/solution/Fe interface. In stage 2, atmospheric CO_2 and O_2 (air) are adsorbed to the interface by removing aliquots of each electrolyte. In stage 3, the surface is completely oxidized in air, after removal of the electrolyte. First, to confirm the Fe surface was clean, a spectrum was collected of the dry Fe surface, shown in black at the bottom panels of Figure 2A-C in the 2000 cm^{-1} – 600 cm^{-1} spectral region. The sample was then half-submerged in nanopure water prior to adding the ionic solutions (water, dark blue spectrum). The signal in the liquid phase was monitored by checking that the p/p interferogram was half the signal from the dry Fe surface. Afterwards, a volume of the water was removed and the stock solutions were spiked into the beaker, thus exposing the iron surface to either 10 mM of A) $MgCl_2(aq)$, B) $KCl(aq)$, or C) $FeCl_2(aq)$, indicated as stage 1 (purple spectra).

For iron in 10 mM $MgCl_2(aq)$ in Figure 2A, no vibrational modes were observed in stage 1, suggesting no chemical reaction occurred yet or was not observed. However, upon removal of 250 µL aliquots, atmospheric O_2 and CO_2 from air adsorbs to the Fe interface and begins to oxidize the surface (stage 2, blue/green spectra), over 132 minutes. After collecting five spectra over 48 minutes, a small δOH mode appeared at 1654 cm^{-1} and increased over time as a result of surface hydroxylation or from the solution.[33, 35] Additional peaks appeared at 1490 cm^{-1}, assigned to νC-

O, and at 860 cm^{-1}, assigned to δCO_3 from surface adsorbed CO_3. Over time, the intensity of the νC-O mode at 1490 cm^{-1} increased and shifted to 1464 cm^{-1} suggesting that surface carbonates are grown on the surface.

In stage 3, the 10 mM $MgCl_2$(aq) solution was completely removed from the analysis spot and the iron surface was allowed to oxidize in air, shown in the top (stage 3, yellow/red) spectra in Figure 2A. Here, the δOH and νCO_3 modes become more intense and split into multiple vibrational modes, indicating a restructuring of the film during oxidation. Four sharp modes are observed at 1652 cm^{-1}, 1529 cm^{-1}, 1460 cm^{-1}, assigned to νCO_3, as well as the δCO_3 mode at 858 cm^{-1}. The doublet at 1478 cm^{-1} and 1450 cm^{-1} are assigned to a monodentate CO_3 mode and the doublet at 1563 cm^{-1} and 1529 cm^{-1} are assigned as a bidentate CO_3 mode.[38] [39] [40] The small peak at 1094 cm^{-1} is assigned to the symmetric νC-O of carbonates,[41] suggesting that adsorbed CO_3 restructures, as the film undergoes crystallization during oxidation in air. These are in agreement with previous studies for Mg carbonate minerals[41], where the primary νCO_3 modes appear between 1515-1320 cm^{-1} for the asymmetric modes and between 1120-1110 cm^{-1} for the symmetric modes[42] as well as key δOH modes between 1650-1575 cm^{-1}.[43] Similar monodentate, bidentate, and polydentate modes were observed from corrosion of Mg surfaces in air, from $Mg(OH)_2$ and $MgCO_3$.[40] [44]

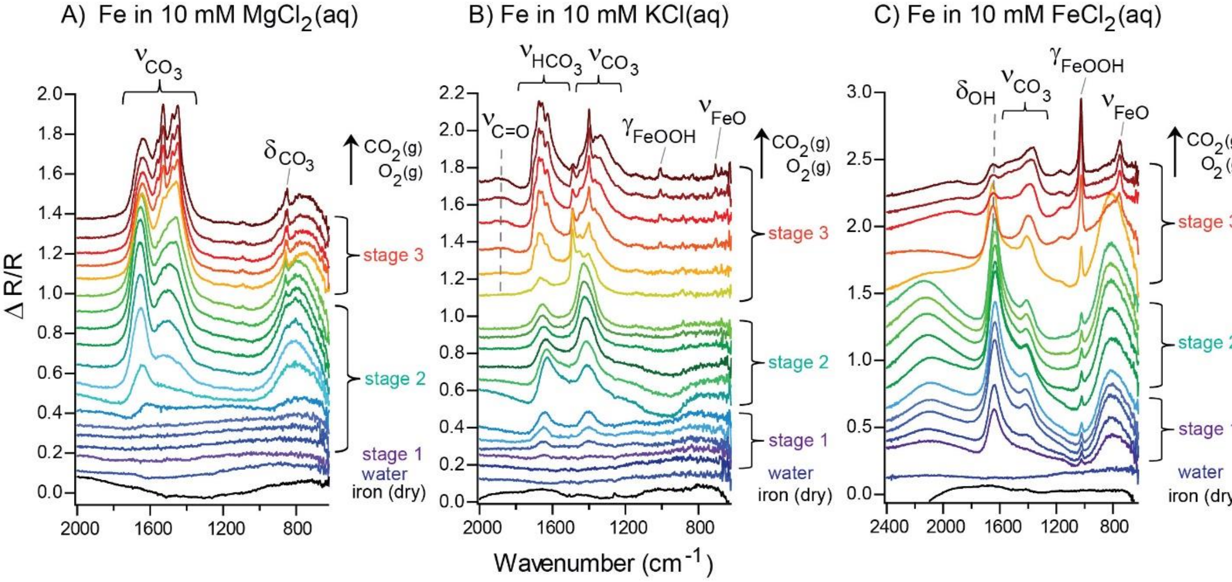

Figure 2: PM-IRRAS spectra of O_2 and CO_2 adsorption to the air/solution/Fe interface in A) 10 mM $MgCl_2$(aq), B) 10 mM KCl(aq), and C) 10 mM $FeCl_2$(aq). Spectra at the air/solution/Fe interface was collected in stage 1. In stage 2, atmospheric O_2 and CO_2 adsorption to the interface followed by oxidation in air in stage 3, which leads to the formation of unique signatures of carbonate films.

Significantly different vibrational signatures are observed at the air/KCl(aq)/Fe interface, shown in Figure 2B. Initially in stage 1, two vibrational modes appear at 1646 cm^{-1} and 1408 cm^{-1}, assigned to δOH and νCO_3, respectively. Both modes increase as a function of time indicating the oxidation at the air/KCl(aq)/Fe interface produces surface adsorbed hydroxylated and carbonate species. In stage 2, during adsorption of atmospheric O_2 and CO_2, the position of the δOH mode remains the same with a decrease in intensity, while the νCO_3 mode shifts to 1432 cm^{-1} and increases in intensity over 62 minutes. These observations are similar to our previous studies of Fe in NaCl(aq), which attributed the δOH mode to the aqueous phase of the electrolyte or surface hydroxylation.[33] This indicates that the hydroxylated species may be consumed as the surface adsorbs CO_2, thus provide basic sites to react with the acidic CO_2 to form surface adsorbed CO_3 or HCO_3 species.

After surface oxidation in stage 3, with complete removal of the KCl(aq) solution, the δOH and νC-O modes increase and sharpen, where the δOH mode blue shifts to 1660 cm^{-1} and the νC-O mode red shifts to 1404 cm^{-1}. New sharp vibrations appear in the red spectra (stage 3) in 2B showing signatures of carbonates: at 1697 cm^{-1}, assigned to νC=O; the 1674 cm^{-1} and 1635 cm^{-1} peaks, assigned to δOH; and the peaks at 1490 cm^{-1}, 1454 cm^{-1}, 1400 cm^{-1} are assigned to νCO_3 (asym). Modes from δCOH appear as a shoulder near 1328 cm^{-1} and increase during oxidation.[38] These peaks shift to 1707 cm^{-1}, 1674 cm^{-1}, 1659 cm^{-1}, 1629 cm^{-1}, 1490 cm^{-1}, 1400 cm^{-1}, in stage 3 due the restructuring of the carbonate film as it crystallizes in air. We attribute the final signature to the formation of a bicarbonate film at the interface.[45-47] Evidence of iron oxidation is also observed from the presence of weak modes of γ-FeOOH at 1012 cm^{-1} and νFe-O at 709 cm^{-1}.

Since the cation in the electrolyte appears to influence the identity of the film grown on the Fe surface, there may be a reason why the Mg^{2+} and K^{+} cations outcompete the Fe^{2+} ions, which dissolve into solution from reduction-oxidation and corrosion of the iron surface.[35] [22] To verify the ion competition, a 3rd benchmark experiment was done in a 10 mM $FeCl_2$(aq) solution (shown in Figure 2C) to compare the competition of cations with that of Fe^{2+}. When the iron surface is first exposed to 10 mM $FeCl_2$(aq) in stage 1, strong and narrow peaks immediately appear at 1645 cm^{-1}, assigned to δOH from the solution or surface hydroxyl groups, and at 1415 cm^{-1}, from νCO_3. Over time, the δOH mode shifts to 1637 cm^{-1} and a small and sharp peak appears at 1025 cm^{-1}, from γ-FeOOH.[33]

After the Fe interface is gradually exposed to atmospheric CO_2 and O_2 (stage 2), the δOH modes remain the same, while the νC-O peaks slowly increase. During air oxidation (stage 3), the δOH mode at 1655 cm^{-1} shifts to 1666 cm^{-1} and the νC-O mode at 1415 cm^{-1} shifts to 1367 cm^{-1}, while νCO_3 appears at 1528 cm^{-1}, from the growth of surface carbonates. As oxidation proceeds, the surface corrodes to form γ-FeOOH, observed at 1027 cm^{-1}, 1172 cm^{-1}, and 756 cm^{-1}.[33] [35] [48] It is interesting that γ-FeOOH has become the dominant surface species during the air oxidation stage, overcoming surface carbonate signals. The Fe^{2+} produced at the interface as a result of Fe^0 oxidation, appear to react with atmospheric CO_2, which initially forms iron carbonate. It is not until oxidation of Fe^{2+} into Fe^{3+} by atmospheric O_2(g) in the presence of the thin water layer that γ-FeOOH is grown and becomes the dominant species at the interface. This suggests that without added cations to adsorb CO_2, iron oxidizes to γ-FeOOH.

3.2: Quantification of Film Growth

In order to determine the effect of the cation on the rate of interfacial hydroxylation and carbonation, the peak areas for each solution were fitted to find the relative coverage of each surface species and plotted as a function of time. The procedure for obtaining the peak areas is described in the methods section. The relative coverage, θ, of each species was measured by taking the ratio of the peak area in stage 1 or stage 2 and normalizing to the maximum peak area in stage 3. These coverages for both the δOH and νCO_3 modes for all 3 solutions are shown in Figure 3A-

F. Each graph in Figure 3 represents hydroxylation (3A-C) and carbonation (3D-F) of the iron interface in stage 1 and 2, when the vibrational modes first appear. Stage 1 for Fe in each electrolyte solution is represented as a negative time scale and stage 2 is shown to the right of the dotted line for the air adsorption stage (begins at 0 minutes). Different iron purities are presented for reproducibility and produce the same vibrational signatures for each solution. The 99.99% (low purity, LP) iron contained anti-corrosion metals that did not corrode the surface as quickly as the as the 99.995% (high purity, HP) iron suggesting that corrosion must occur prior to film growth. It was determined that trace (anti-corrosive) metals in LP iron altered the adsorption kinetics by delayed film growth (shown in Table S1 and S2 in the SI).

Figure 3A and 3D compares the rate of interfacial hydroxylation and carbonation of Fe (low purity-99.99% and high purity-99.995%) in 10 mM $MgCl_2$(aq), shown as the open and closed green triangles, respectively. Surface hydroxylation of Fe does not begin in $MgCl_2$(aq) until atmospheric O_2 and CO_2 are adsorbed to the interface region in stage 2. Fe in $MgCl_2$(aq) follows the same trend as in the $CaCl_2$(aq) (see Figure S2 in SI), where initially, the surface hydroxylation is not observed in stage 1, but after 20-40 minutes of air adsorption in stage 2, the coverage increases until it reaches a saturation point, between 40-80 minutes.[33] The interfacial carbonation follows the same trend between 0-40 min in Figure 3D as atmospheric O_2 and CO_2 are gradually adsorbed to the solution/Fe interface, where the film growth saturates by 40 min.

For Fe in KCl(aq) (yellow diamonds) in Fig 3B, the coverage of δOH increases linearly in stage 1 until air adsorption begins, at 0 min in stage 2. This trend is similar to our previous observations for Fe in NaCl(aq), where δOH appeared from surface hydroxylation.[33] During stage 2, O_2 and CO_2 is adsorbed to the interface, the hydroxyl coverage increases and plateaus between 40-70 minutes. Around the same time, the carbonation rate increases continuously in Fig 3E. This trend may be due to the surface sites are saturated with hydroxyl groups and dissolved CO_2 begins to react with the hydroxyl groups to form carbonates. The carbonation continues in an upward trajectory, unlike for the dication solutions.

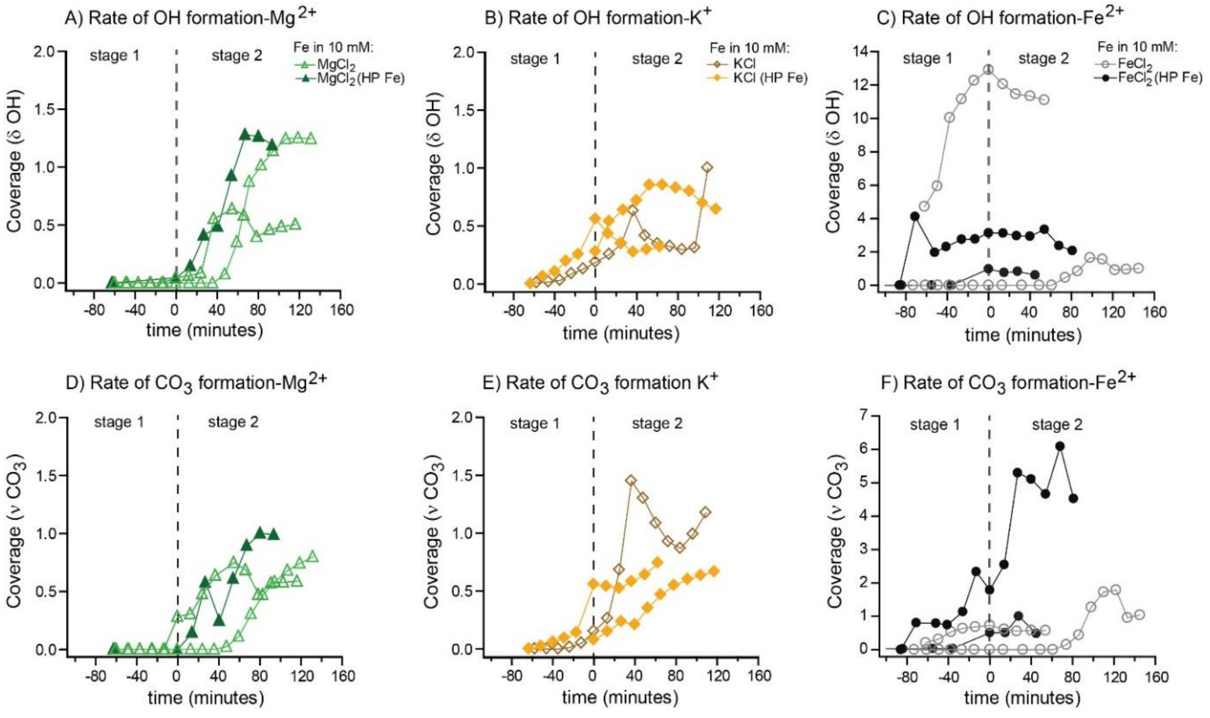

Figure 3: Coverage profiles for the δOH and νCO$_3$ modes plotted over time from adsorption of atmospheric CO$_2$ and O$_2$ yield the rate of hydroxylation and carbonation of the iron interface in the electrolytes in stages 1 and 2. Interfacial hydroxylation of Fe in A) MgCl$_2$(aq) (green triangles), B) KCl(aq) (yellow diamonds), and C) FeCl$_2$(aq) (gray circles). Interfacial carbonation of Fe in D) MgCl$_2$(aq), E) KCl(aq), and F) FeCl$_2$(aq). Closed markers were obtained on high purity (99.995%, HP) Fe and open markers were obtained on 99.99% Fe.

For Fe in FeCl$_2$(aq), the hydroxylation begins immediately in stage 1, in Figure 3C, and plateaus during stage 2 when O$_2$ and CO$_2$ is adsorbed to the interface region. This is different than observed for the other alkali and alkaline electrolytes. Iron oxidation expected in FeCl$_2$(aq) as the surface undergoes a redox reaction in a mildly acidic solution, where Fe^{2+} easily oxidizes to Fe(OH)$_2$. The carbonation rates, in Figure 3F, indicate that initially carbonate growth occurs in stage 1, but the rate slows in stage 2, during CO$_2$ adsorption. After the solution is removed, oxidation takes over in stage 3 to form the γ-FeOOH layer, as shown in Fig 2C. This suggests that atmospheric O$_2$ is a stronger oxidant on iron surfaces, thus producing the γ-FeOOH film over FeCO$_3$.

To quantify the rates of hydroxylation and carbonation, the linear rise in the δOH coverage or νCO$_3$ coverage in stages 1 and 2 were estimated using a 1st order approximation. The natural log of the initial rise of the coverage was plotted over time to find the rates in s^{-1}. Table 1 below shows the rates for high purity (HP) iron for each type of electrolyte, in comparison to the rates from our previous experiments in ref [33]. These were computed separately as the low purity Fe samples have traces of anti-corrosion resistant metals, which change the kinetic rates (see Table S2 in the SI).

For HP iron, the rate of hydroxylation and carbonation was only observed in stage 1 for the K$^+$, Na$^+$, and Fe^{2+} chloride solutions. In this stage, the surface becomes hydroxylated as it corrodes and a small amount of atmospheric O$_2$ and CO$_2$ can diffuse into solution and react at the liquid/iron interface. Here the rates are shown to increase in the order of Na$^+$ > K$^+$ > Fe^{2+}. In the case for NaCl(aq), the δOH mode was assigned to either the liquid solution or surface hydroxylation, which disappears during stage 3, and only FeCO$_3$ modes were observed.[35] For Fe in KCl(aq), the δOH mode remains on the surface during stage 3 in Figure 2C and is converted to bicarbonate, which alters the hydroxylation rate. Peaks were not observed for the Mg and Ca[33] chloride solutions, suggesting that hydroxylation or carbonation do not occur in stage 1 or are not detected, as shown in Figure 2A.

Table 1: Rates of hydroxylation and carbonation (s^{-1}) of iron surfaces exposed to each solution.

HP (99.995%) Fe	**stage 1**		**stage 2**	
solution	**δOH**	**νCO$_3$**	**δOH**	**νCO$_3$**
MgCl$_2$	n/a	n/a	7.94×10^{-4}	4.22×10^{-4}
CaCl$_2$	n/a	n/a	7.88×10^{-4}	9.19×10^{-4}
KCl	6.88×10^{-4}	8.53×10^{-4}	1.00×10^{-6}	2.21×10^{-4}
NaCl	1.22×10^{-3}	1.43×10^{-3}	2.21×10^{-4}	3.57×10^{-4}
FeCl$_2$	1.50×10^{-4}	3.22×10^{-4}	-1.14×10^{-4}	1.19×10^{-4}

It is not until stage 2, where O_2 and CO_2 adsorbs to the solution/Fe interface that the rate of carbonation increases and the rate of hydroxylation decreases for Mg^{2+}, Ca^{2+}, K^+, and Na^+. The decrease in hydroxylation rate may imply that the surface OH groups react with CO_2 or dissolved HCO_3^- (produced from carbonic acid equilibrium) and are converted into surface carbonate species. For HP Fe surfaces, the rate of carbonation increases in the order of $Ca^{2+} > Mg^{2+} > Na^+ > K^+ > Fe^{2+}$, shown in Table 1, in agreement with previous studies that find that Ca and Mg materials have high rates of CO_2 adsorption.[27 49 50] The rate of carbonation is low for iron exposed to $FeCl_2$(aq) as the surface is shown to oxidize to form γ-FeOOH. It should be noted the dication solutions have twice the amount of chloride as the monocationic solutions. The Cl^- ions have been shown to pit the iron surface[33, 51-53], initiating the redox reaction, releasing iron into the solution. This suggests that twice as much chloride may lead to more pitting and corrosion of the surface, creating nucleation sites for higher rates of carbonate growth. The surface corrosion is discussed below in the AFM results.

3.3 Identification of mineral films using ATR-FTIR analysis

To confirm the identity of the films produced on Fe interface, the ATR-FTIR spectra were collected of the Fe surfaces after the PM-IRRAS experiments of the interface region. The ATR-FTIR spectrometer was also used to measure the regions completely submerged in electrolyte, that were not achievable with PM-IRRAS. In addition, PM-IRRAS is more surface sensitive, measuring the top ≈ 0.4 μm of the (iron) surface, while the ATR-FTIR configuration measures up to 2 μm in depth (shown in Fig 1). The spectra of these regions were compared with the ATR-FTIR spectra of natural mineral samples that were used as standards to identify the films grown on the different regions of the samples, as shown in Figure 4 in panels I-III as well as in Figure S3 and Table S3 in the SI.

The ATR-FTIR spectrum of the iron interface exposed to A) 10 mM $MgCl_2$(aq) is compared with spectra of B) magnesite ($MgCO_3$), and C) hydromagnesite ($Mg_5(CO_3)_4(OH)_2.4H_2O$), D) Pokrovsite ($Mg_2(CO_3)(OH)_2$), and E) nesquehonite ($Mg(HCO_3)OH{\cdot}2H_2O$, shown in Panel I. Three characteristic modes for A) Fe in 10 mM $MgCl_2$(aq) at 1609 cm^{-1}, 1535 cm^{-1}, and 1445 cm^{-1} confirm the surface carbonates/bicarbonate species at the interface region.[48] Two additional modes at 1093 cm^{-1} and 855 cm^{-1}, represent the asymmetric νCO_3 and the δCO_3 deformation modes, respectively. These peaks align best with the characteristic νCO_3 modes of B) magnesite and C) hydromagnesite, D) Pokrovsite, and E) nesquehonite.[54 42] The broad νOH peak within the 3500 – 3000 cm^{-1}, assigned to hydroxyl species (Fe-OH/Mg-OH) and the νMgO mode between 680-600 cm^{-1} in spectrum A, can be used to differentiate the potential matches with the mineral spectra. These modes are only present in spectra of C) hydromagnesite, E) nesquehonite, and in Brugnatellite, ($Mg_6Fe^{3+}(CO_3)(OH)_{13}{\cdot}4H_2O$, in Figure S3 in SI). This analysis suggests the film grown at the air/$MgCl_2$(aq)/Fe interface is comprised of a mixture of magnesite, hydromagnesite, and a Mg hydroxy carbonate.

The identity of the film grown at the air/KCl(aq)/Fe interface, spectrum F, was found by comparing it to the ATR-FTIR spectra in panel II of: G) a 10 mM $KHCO_3$ droplet that was air-dried on a new polished Fe surface, H) natural Erythrosiderite ($K_2[FeCl_5(H_2O)]$), I) potassium carbonate powder (K_2CO_3), and J) the polished iron surface. Spectrum F shows vibrational signatures of an δOH at 1635 cm^{-1}, the νHCO_3 at 1394 cm^{-1}, a δCOH at 1251 cm^{-1}, a νC-O at 1012 cm^{-1}, and δCO_3 at 835 cm^{-1}. Neither spectrum H nor I are an exact match for the film grown on iron. The vibrational modes in H) Erythrosiderite has broad νOH modes, strong δOH deformation modes at 1060 cm^{-1}, and a unique mode at 1639 cm^{-1} that is aligned with spectrum F. Spectrum I of a KCO_3 powder, shows the νCO_3 at 1360 cm^{-1} and the δCO_3 at 878 cm^{-1} that only match a few of the peaks in F. The clean polished iron surface (spectrum J) is shown for comparison indicating no Fe oxidation or mineral formation, as expected. Spectrum F aligns best with spectrum G of a 10 mM $KHCO_3$ solution drop and dried on a different iron surface. The key signatures indicate a potassium-rich bicarbonate film that is grown into the surface.[38] For the Fe interface exposed to $FeCl_2$(aq) in spectrum K in Panel III, the signatures are similar to spectrum P of γ-FeOOH (lepidocrocite). Nonspecific carbonate modes are also observed at 1627 cm^{-1}, 1478 cm^{-1}, and 1351 cm^{-1}.[33, 55] This shows the γ-FeOOH is the primary film grown on the surface with a small contribution from a hydroxy carbonate film. Overall, signatures of cation specific carbonate films are grown at the interface region in agreement with other cation rich carbonates, iron in NaCl(aq) or $CaCl_2$(aq).[33]

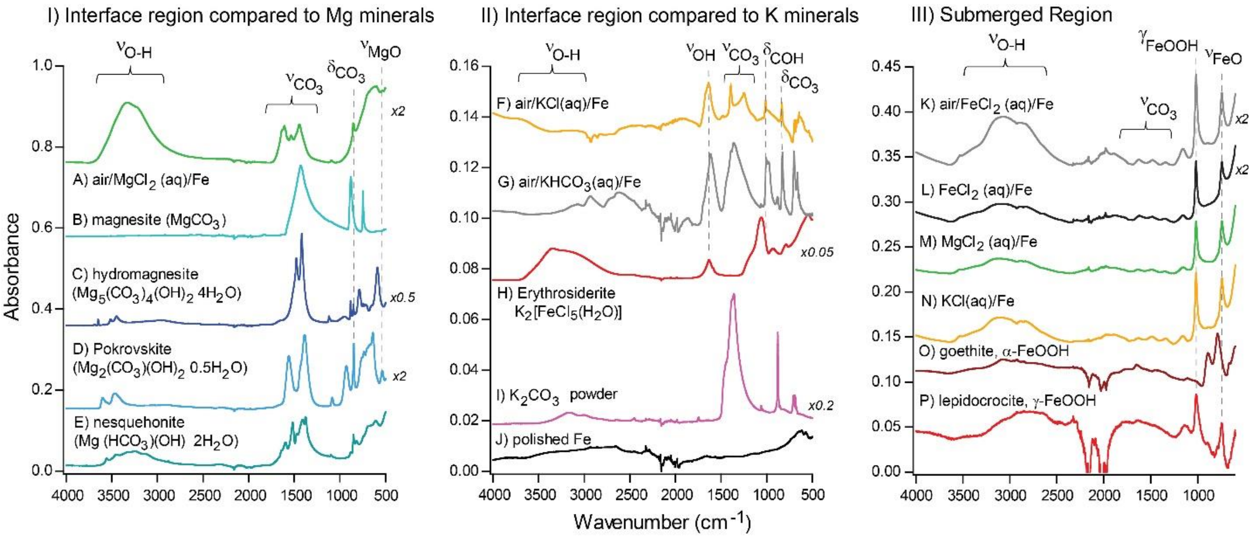

Figure 4: ATR-FTIR spectra of carbonate films grown on Fe: I) the Fe interface exposed to A) $MgCl_2$(aq) compared to B-E) Mg mineral specimens, II) Fe exposed to F) KCl(aq) compared to G-I) mineral specimens and the J) polished Fe surface. Corroded surfaces are compared in III) of the K) interface of Fe exposed to $FeCl_2$(aq) along with the submerged regions of iron in L) $MgCl_2$(aq), M) KCl(aq), N) $FeCl_2$(aq), and O-P) iron oxyhydroxide minerals. Spectra O and P are reprinted (adapted) with permission from de Alwis, C.; Trought, M.; Lundeen, J.; Perrine, K. A. Effect of Cations on the Oxidation and Atmospheric Corrosion of Iron Interfaces to Minerals. *Journal of Physical Chemistry A* **2021**, *125* (36), 8047-8063. Copyright 2021 American Chemical Society.

The corroded regions submerged in the electrolyte solutions, where the sample was not gradually exposed to atmospheric O_2 and CO_2, was also assessed and shown in panel III. The ATR-FTIR spectra of iron in, L) 10 mM $FeCl_2$(aq), M) 10 mM $MgCl_2$(aq), and N) 10 mM KCl(aq) are remarkably similar compared with the spectra of Fe oxyhydroxide mineral specimens, O) goethite (α-FeOOH) and P) lepidocrocite (γ-FeOOH).[33] The spectra (K-N) show almost identical vibrational modes to that of spectrum P) of γ-FeOOH (lepidocrocite), with broad νOH modes within 3500 – 2500 cm^{-1}, along with Fe-O modes at 1155 cm^{-1}, 1016 cm^{-1}, and 745 cm^{-1}.[35 55] Also, spectra (K-N) show three weak νCO_3 modes between 1622-1630 cm^{-1}, 1482-1487 cm^{-1}, and 1340-1350 cm^{-1} originating from adsorbed nonspecific carbonates in the submerged regions. The intensities of these three peaks are analogous to the spectral features in Figure 2C and spectrum K of the interface region of Fe exposed to $FeCl_2$(aq), where the same carbonates are observed. Other studies have shown similar vibrational modes resemble those of *in situ* gas phase CO_2 adsorption on ferrihydrite.[45] This suggests that the Fe^{2+} cation dominates the mineral composition in solution in the submerged region, where the reaction occurs with dissolved O_2 and HCO_3 species. It also suggests the Mg^{2+} and K^+ do not significantly contribute in the mineral growth in the submerged region on the Fe surfaces.

Other regions submerged in the electrolytes that did not corrode were also assessed, shown in Figure S4 in the SI, where non-specific carbonate species were observed. This suggests an intermediate carbonate adsorbs to the surface prior to formation of distinct carbonate films. No traces of dissolved carbonates were observed in the ATR-FTIR spectra of the solutions after the PM-IRRAS experiments (shown in Figure S5). The majority of the samples produce γ-FeOOH in the corroded area in the submerged regions, so we focus our discussion on this species, present on all the samples.

3.4 Elemental Composition of the Interface and Submerged Regions by XPS

To measure the relative composition and changes in the metal binding of the iron films after surface oxidation and corrosion, XPS was used to assess the top 10 nm of the surface. The C1s and the O1s region are shown in Figure 5I-IV that confirm the formation of carbonate at the interface regions. Each panel shows four XPS spectra that were collected on the A) droplet interface of Fe exposed to 1 mM $MgCl_2$(aq) or KCl(aq) solutions from the AFM experiments as well as different regions of the samples after PM-IRRAS experiments from exposure to 10 mM solutions: B) the interface, C) the submerged region, and D) the unexposed, polished region.

In all spectra in panel I of the C1s region of Fe exposed to $MgCl_2$(aq), the following species were observed: adventitious carbon (C-H) at 284.5 eV, C-O at 286.0-286.3 eV, and C=O at 287.8 eV. On the interface region (spectrum B) additional carbon species of carbonate (CO_3) at 289.1-289.9 eV and HCO_3 at 293.0 eV were detected from the adsorbed carbonate film. In the submerged regions only a residual amount of CO_3 at 290.5 eV was observed. The amount of CO_3 and HCO_3 on the interface region is significantly higher than the other regions of the corroded Fe surface due to the film growth.

For iron exposed to KCl(aq) in panel III, the same three species along with leftover K ions are observed at the interface in the C1s region. Carboxylate species are present at 288.6 eV, attributed to carbonate, along with adventitious hydrocarbons at 284.5 eV and C-O at 286.8 eV. The $K2p_{3/2}$ region at 292.8 eV overlaps with the carbonate and bicarbonate species of the C1s region, but the carbonate/carboxylate species are larger at the interface region compared to the C) submerged region and D) polished iron. After rinsing the surface with nanopure water (spectrum A), the K^+ and the carbonate species remain on the surface, suggesting that it is grown into the carbonate film, in alignment with the PM-IRRAS and FTIR spectra. The submerged region displays a smaller concentration of carbonates with some remaining KCl ($K2p_{3/2}$ at 292.3 eV and $K2p_{1/2}$ at 295.1 eV). These regions show evidence of carbonate deposition compared to the unexposed, polished area of the Fe surface, where no carbonates or other elements were detected.

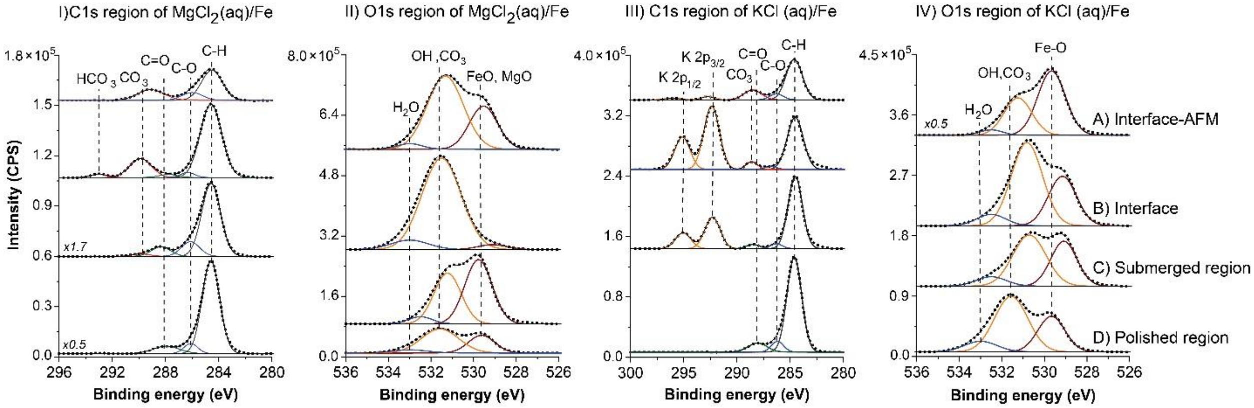

Figure 5: XPS spectra of Fe oxidized in 10 mM $MgCl_2$(aq) in the I) C1s region and the II) O1s region compared with Fe oxidized in 10 mM KCl(aq) for the III) C1s region and the IV) O1s region. Spectra across each panel row: A) the interface region from the samples in the AFM experiments, and regions from the PM-IRRAS experiments: B) the interface region C) region submerged in solution, and D) the polished iron surface. Results show a large concentration of carbonates (HCO_3 and CO_3) at the interface relative to other oxidized species (Fe-O) and other surface regions.

XPS spectra of the O1s region is shown in Panel II, for Fe oxidized in 10 mM $MgCl_2$(aq) and in panel IV, for Fe oxidized in 10 mM KCl(aq). The O1s region mirrors the spectra of the C1s region, where a large concentration of carbonates (CO_3) are present at the interface region between 531.2-531.5 eV. Two additional oxygen species are present at the interface (spectra A and B) from oxides (Fe-O or Mg-O) at 529.7 eV and adsorbed water (H_2O) at 532.5-533.0 eV. The peak at 531.5 eV for $MgCl_2$ and 530.8 eV for KCl is the largest contribution, attributed to both Fe-OH and surface CO_3, as their binding energies overlap.[56, 57] Even after rinsing the surface with water (spectrum A), a high amount of hydroxide/carbonate (531.3 eV) species remains chemically adsorbed to the surface after exposure to $MgCl_2$(aq). For Fe exposed to KCl(aq), the CO_3 peak decreases relative to the Fe-O peak after rinsing likely due to the dissolution of the bicarbonate film. The same oxygen species are also present in the submerged region (spectrum C) but in different ratios indicating the surface was oxidized after corrosion. These ratios are different than Spectrum D of the polished (non-corroded) region where only Fe-O, Fe-OH, and adsorbed water species are present from the native oxide layer that covers iron. The results confirm a higher carbonate formation at the interface regions (A-B) compared to the region submerged in solution (C) and the polished Fe surface (D) that show little carbonate growth. This indicates that the air/$MgCl_2$(aq)/Fe interface has a unique ability of growing carbonate species compared to the other areas of the Fe surface, in agreement that Mg carbonate films have the larger absorption rate but Ca has the higher absorption capacity.[44, 58]

Other XPS spectra of the Mg 1s, Mg 2p, Fe 2p, and Cl 2p regions are shown in Figures S6-S8 in the SI for the areas of the samples presented above. Only Mg carbonate was identified on the surface. Remnants of the Cl^- species from the ionic solutions were present in the regions exposed to the electrolytes in all regions near 198.0 eV. A second species is observed at 198.9 eV from Fe-Cl only at the interface region, suggesting chloride binding to the iron surface. No other significant shifts in binding energy were observed in these regions showing that the ions remain on the surface after surface oxidation and corrosion.

To find the relative concentration of the ions at each region, the peak areas from the XPS spectra were used to compute the elemental ratios of the iron surface exposed to the KCl(aq) and $MgCl_2$(aq) after the PM-IRRAS experiments. These results, shown in Table 2, are compared with our previous results, NaCl(aq) and $CaCl_2$(aq) and with $FeCl_2$(aq).[33] Elemental ratios describe the relative composition adsorbed carbonate (HCO_3 and CO_3), cations (Mg^{2+} and K^+), and Cl^- anions at the interface compared to the region submerged in solution and the polished Fe prior to any solution. Each peak area was normalized to the total area of the Fe 2p region.

The interface is shown to have 3-5 times higher relative concentration of carbonates for $MgCl_2$(aq), KCl(aq), $CaCl_2$(aq), and NaCl(aq) compared to the submerged region. The polished Fe and Fe exposed to $FeCl_2$(aq) has oxide layers present on the surfaces and shows low relative concentration of carbonates. There is also a corollary high cation/Fe ratio along with the carbonate formation, further indicating cation specific carbonate films are grown at the interface region. A similar trend is observed for the Cl^-/Fe ratio.[33] This suggests that because more Cl^- ions are present at the air/solution interface, more pitting occurs, thus increasing nucleation sites for a higher rate of favorable film growth. This data and the chemical identity of the films in the PM-IRRAS and ATR-FTIR spectra suggests that cation- specific carbonate films are grown at the interface region.

Table 2: Elemental ratios quantifying the total carbonate (HCO_3 and CO_3), cation, and anion (Cl^-) concentrations on different areas on iron.

Solution	**Region on Fe sample**	**Total carbonate (C1s)/Fe2p**	**Cation/Fe2p**	**Cl2p/Fe2p**
$MgCl_2$(aq)	Film	6.98	19.26	5.75
	Interface	0.72	0.99	0.58
	Submerged	0.13	0.20	0.13
KCl(aq)	Interface	0.79	2.14	0.26
	Submerged	0.26	0.48	0.08
$CaCl_2$(aq)	Interface	2.24	4.14	3.99
	Submerged	0.61	0.96	0.38
NaCl(aq)	Interface	1.41	1.74	0.10
	Submerged	1.07	1.54	0.09
$FeCl_2$(aq)	Interface	0.08	1.00	0.04
	Submerged	0.11	1.00	0.05
none	polished Fe	0.01	0.04	0.07

Overall, the data in Figure 4 and 5 as well as Table 2 indicate that cation-specific carbonate films are grown at the interface region on Fe in $MgCl_2$(aq) and KCl(aq). Whereas the product in the region submerged in solution is a mixture of γ-FeOOH with an iron hydroxycarbonate, similar to what was observed for Fe in $CaCl_2$(aq) and NaCl(aq).[33] Together these results confirm cations influence the identity of the mineral film growth at the air/electrolyte/Fe interface.

3.5 *In situ* AFM – measure of apparent corrosion rate

To determine the effect of the ions on the physical changes of the iron surface, *in situ* liquid AFM was used to measure the topographical changes surface roughness (RMS), as a measure of the apparent corrosion rate. A sample of polished HP iron was imaged *ex situ* prior to electrolyte exposure to check the surface roughness, as shown in Figure 6A. The iron surface was then exposed to a droplet of 1 mM $MgCl_2$(aq). Images in the same area were collected over time as the surface corroded, shown on the top row of Figure 6B-D, for a period of 140 minutes. A similar experiment was repeated for the HP iron surface in 1 mM KCl(aq), shown on the bottom row of Figure 6F-H. Images shown represent the beginning, middle, and end of the corrosion process.

In situ imaging of the sample allows corrosion to be observed in real-time. The first images were recorded 40-46 minutes into exposure of the iron surface to the electrolyte droplets, as shown in images B and F. After 120 minutes, larger features are produced on the surface (images B-D) with the height scale between 115 nm to 125 nm for iron in 1 mM $MgCl_2$(aq) compared to 4 nm features in images A and E. This is attributed to the surface roughening during the corrosion process, which consists of dissolution of Fe species and subsequent redeposition of particulates on the surface. For iron in 1 mM KCl(aq), the surface features remain the same height between 70 nm-150 nm during the time frames that were imaged (Images 6F-H). For visual comparison of the gradual corrosion, see photos and additional images in Fig. S9 in the SI.

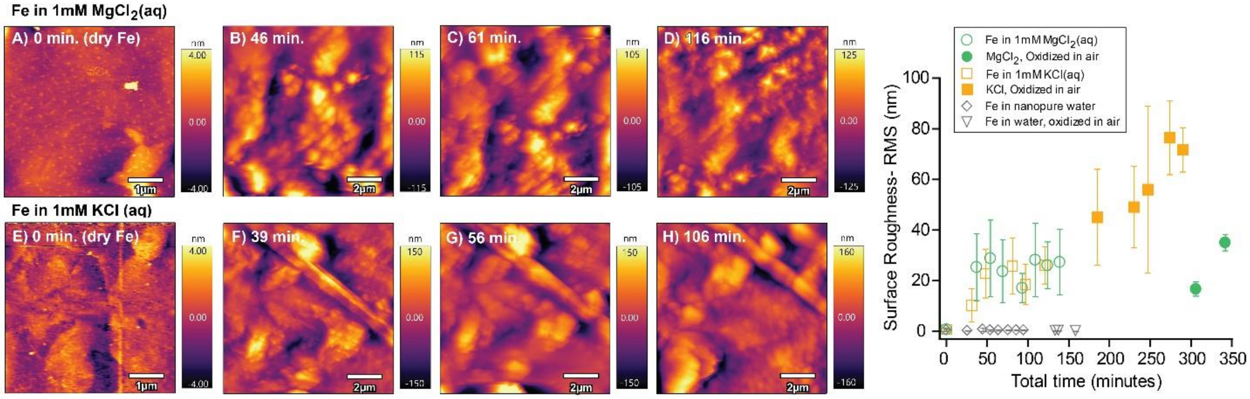

Figure 6: AFM images of iron before corrosion (A and E) and during corrosion over time for iron in (B-D) $MgCl_2$(aq) compared to iron in (F-H) KCl(aq). Images A and E were collected in a different location prior to applying the electrolytes. Plot of the surface roughness (RMS) is shown as an apparent rate of corrosion for HP Fe in 1 mM $MgCl_2$(aq) (green circles), Fe in 1 mM KCl(aq) (yellow squares), and Fe in nanopure water (gray diamonds). Closed markers are for the same sample after it was rinsed in nanopure water and oxidized in air.

In Figure 6, the surface roughness (in RMS) of iron was plotted over time (in minutes) to estimate the apparent rate of corrosion. The RMS values increase over time for iron in either 1 mM $MgCl_2$(aq) (green circles) or 1 mM KCl(aq) (yellow squares) compared to iron in nanopure water (gray diamonds). The RMS value of the iron surface before being exposed to solution was 0.90 nm. After exposure to the electrolyte solutions, the surface roughness gradually increased to 26 nm in $MgCl_2$(aq) compared to 10 nm in KCl(aq). This suggests, initially, $MgCl_2$(aq) corrodes the iron surface 2x faster than in KCl(aq). This is attributed to the amount of Cl^- present in $MgCl_2$(aq) is twice that of KCl(aq) in equimolar solutions, which pit the surface and initiate corrosion. After the droplet is rinsed off the iron surface and oxidized in air (closed markers), the average roughness for iron exposed to KCl(aq) increases to 45 nm and continues to grow past 70 nm as the surface oxidizes, whereas for Fe in $MgCl_2$(aq) the RMS saturates near 35 nm. The surface corrosion and roughening plateaus in both solutions by 37-48 minutes.

Our previous results were similar for iron in 5 mM $CaCl_2$(aq) where the iron roughness also increased to 30 nm in the same time period. However, for Fe in 5mM NaCl(aq), the roughness was on average < 10 nm, which suggests that at the liquid/Fe interface the cations do not directly affect in the initial stages of surface corrosion. During air oxidation (at the air/Fe interface) the cations may affect the subsequent film growth rate on iron. Studies have found that stainless steel, an iron alloy, corrodes in solutions of KCl, K_2CO_3, and K_2SO_4 due to the formation of potassium chromate, thus freeing up the iron sites for oxidation.[59, 60] In these solutions, Cl^- and CO_2 form HCl or carbonic acid, which can directly attack the iron sites. Additionally, a review determined Mg and Ca cations do not directly participate in steel corrosion, but increase the corrosion rates.[61] These results suggest that the cation role in direct corrosion is unlikely and in our case, pitting events are initiated by the Cl^- anions.

3.6 AFM of mineral formation

The surface morphology variations also give insight into corrosion and film growth. The morphology of the iron surfaces after reaction in the 1mM electrolytes was imaged using *ex situ* AFM. These images are shown in Figure 7 of the different regions in the samples produced from the PM-IRRAS experiments (A-D) compared to samples used in the AFM experiments (E). The images from the *in situ* AFM experiments were collected after the surface was rinsed with nanopure water and dried in air for 1+ hours, thus oxidizing the surface from exposure to atmospheric O_2 and CO_2. Differences in the surface topography are observed of the various regions of the sample: A) the clean, polished region of the iron surface, B) the interface region of the PM-IRRAS samples, C) below the interface, D) area submerged in the solution, and E) select areas from the *in situ* liquid AFM experiments. The left column shows images from iron exposed to $MgCl_2$(aq) and the right column show images from iron exposed to KCl(aq). The RMS values for the AFM experiments are shown as the closed markers in Figure 6.

The polished regions of the iron surfaces (A) are relatively smooth (< 6 nm in height) compared to the white-colored films grown at the interface region (B). The uniform features that are grown at the interface range in height between 20-80 nm suggest that the films are relatively flat from Mg hydroxycarbonate and K bicarbonate deposition. Below the interface region (C), the iron surface appears to have pitting, where small nano-sized features are observed between 30-50 nm in height. This region is directly exposed to the electrolyte, where perhaps the Cl^- ions pit the surface, but lack air exposure for further film formation where nucleation begins. ATR-FTIR spectra of this intermediate region, shown in Figure S4 in the SI, show non-specific carbonates and suggest the beginning stages of film growth.

The submerged regions (D) have significantly larger features well above 400 nm in height from the more severely corroded regions from the PM-IRRAS experiments, after exposure to 10 mM electrolytes and several days of air exposure. There is no significant difference in the topographies of the iron surfaces that were treated with $MgCl_2$ or KCl, suggesting that the physical features after corrosion are not determined by the type of cation. During the initial stages of corrosion in 1mM solutions in (E), similar features are also observed on the samples after air oxidation. These images display stringy-like features[33] [62], similar to the morphology of lepidocrocite on the surface, in agreement with the ATR-FTIR spectral signatures in Figure 4. Hexagonal platelets are also present in images E, which suggest that an iron hydroxy carbonate, synonymous with green rust[63 64], was grown on the surface, similar to our previous findings of iron exposed to $CaCl_2$(aq) and NaCl(aq).[33] This indicates that the cations from the electrolytes do not influence the morphology changes on the iron surface in the submerged region. The ions do appear to influence the RMS values, presumably from film growth, shown in Figure 6. The RMS for the Fe exposed to KCl(aq) continues to increase at a faster rate, while Fe in $MgCl_2$(aq) plateaus, suggesting that the Fe exposed to KCl continues to oxidize and corrode Fe over time.

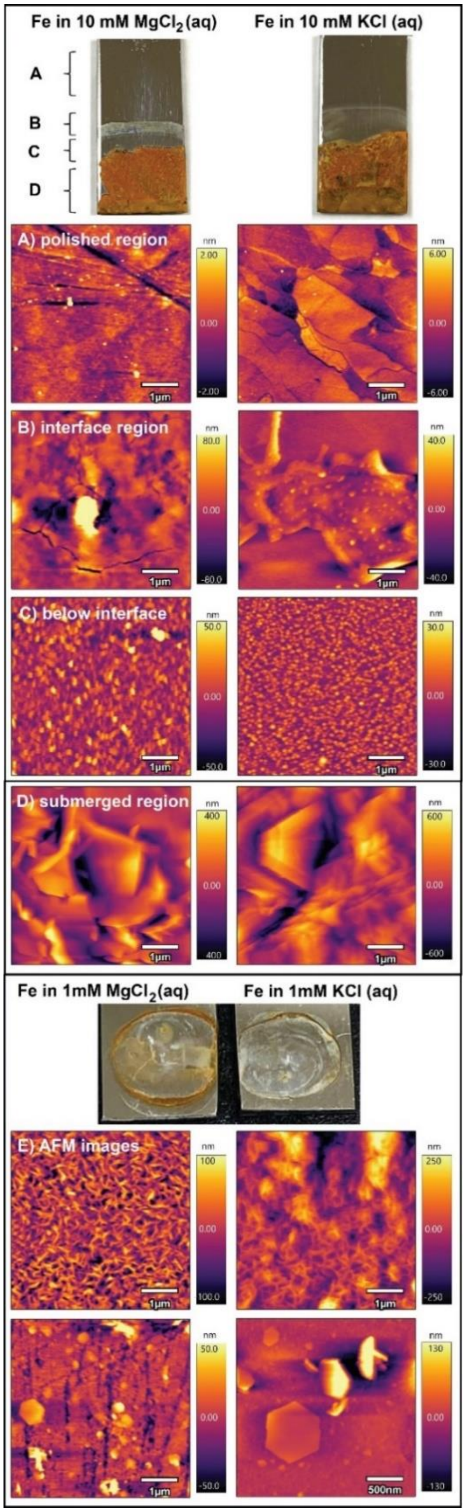

Figure 7: AFM images of different regions of the iron surfaces after air oxidation and corrosion in $MgCl_2$(aq) and KCl(aq): A) polished iron surface, B) interface region, C) below the interface region, D) the submerged region in 10 mM solutions from the PM-IRRAS experiments, and E) regions submerged in 1 mM solutions from the AFM experiments.

3.7 Mechanism of CO_2 capture and mineralization

The results presented above show that the carbonate film identity is specific to the type of cation in the electrolyte at the air/solution/iron interface and is initiated by surface corrosion. A suggested mechanism is summarized in Figure 8. In the first part of the mechanism, corrosion is needed to produce active sites before mineral films can be grown on iron surfaces, as shown from the PM-IRRAS results and the AFM measurements. In steps 1-2) surface corrosion is initiated by the chloride anions through pitting of the native oxide layer on the iron surface[53], thus creating defects that act as nucleation sites for film growth,[65] according to the surface roughness measurements. This then allows for 2) reduction-oxidation to occur followed by hydroxylation of the surface.

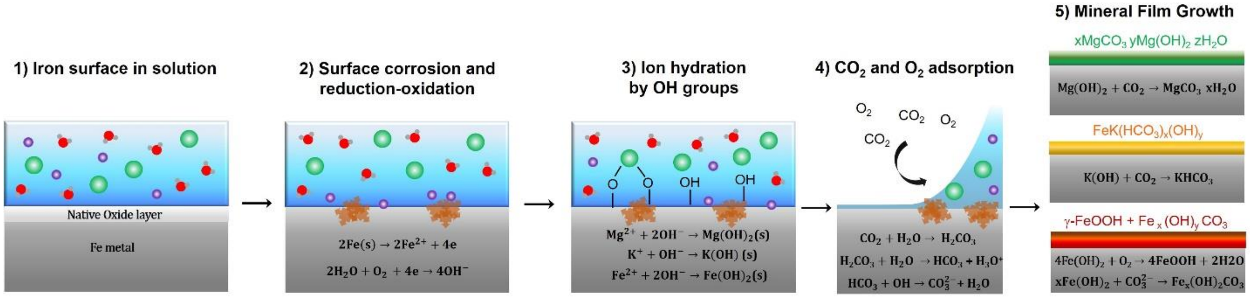

Figure 8: Summary of surface mechanism linking corrosion, CO_2 adsorption, and surface carbonation to form cation specific carbonate films at the air/solution/Fe interface. Atom color scheme: chloride anion (purple), cation (green), oxygen (red), hydrogen (gray).

Once these defect sites are created, they can become hydroxylated in aqueous solutions[66], where the surface hydroxyl groups are predicted to have higher reactivity than OH groups on the hydration shells of dissolved ions.[31] [23] In step 3) these surface OH groups bind with the cation (Mg or K) and also act as basic sites for reaction with the acidic CO_2, as illustrated in Figure 8. Studies have shown that CO_2 adsorbs to defect sites[67], such as the preference for defected MgO(111) produced from high temperature sintering or activated CaO by humidity exposure.[68] On Fe alone, various facets of Fe single crystals are more favorable for CO_2 adsorption due to their high surface area.[69] [70] [71] Defects on oxide surfaces, calcined particles, and 3-dimensional materials have also been shown to increase rates for CO_2 adsorption. [6] [32] Evidence for the surface mediated reaction here is shown from the hydroxyl bending modes from the surface OH groups that were observed for some of the electrolytes. In Figure 3A and 3C the hydroxylation rates follow the order $Na^+ > K^+ > Fe^{2+}$, where these modes are present at the air/solution/Fe interface but disappear as the surface is oxidized and carbonate is grown.

It is possible the OH groups on the hydration shell of the cation could react with CO_2 through complexation prior to particle nucleation and then deposit on the surface.[72-74] This may explain why the OH modes are not observed in stage 1 for $MgCl_2(aq)$ and $CaCl_2(aq)$, but carbonate films are grown at the highest carbonation rates. The OH groups and the defects on the iron surface, must be present for the mineral film growth. Our previous results in nanopure water have shown that no carbonate film growth is observed without added Cl^- ions.[35] The Cl^- pit through the native oxide layer, dissolving Fe^{2+} into solution and exposing Fe^0 and Fe^{2+} sites for further reactions. These studies support our findings that defect sites, produced from iron surface corrosion, and the formation of surface hydroxyl species[75] enable facile adsorption of CO_2 during oxidation.

Secondly, the cation in the electrolyte influences the identity of the carbonate film and the rate of carbonation. In step 4) in Fig. 8 as CO_2 dissolves into solution and the surface begins to oxidize from adsorption of atmospheric O_2 and CO_2, the equilibrium of carbonic acid quickly produces bicarbonate, which can then go on to react with the defect sites or OH groups. Our data show that in step 5) magnesium hydroxy carbonates are formed for Mg^{2+}, but potassium-rich bicarbonate was grown from exposure to K^+, and only carbonates were produced for Na^+ and Ca^{2+}. Since the carbonates have a high concentration at the interface region, this is attributed to the exposure of the solution to CO_2 in air. Although the formation of dissolved bicarbonate from carbonic acid equilibrium[76] is faster than direct CO_2 adsorption at the gas/solid interface, the relatively high concentration of dissolved CO_2 and conversion to HCO_3 and CO_3 species[77] at the interface region has a larger effect on the carbonate film formation. This is shown in the XPS elemental ratios where higher relative concentrations of the cations, carbonates, and chlorides are observed at the interface region. The ATR-FTIR spectroscopy analysis identify the cation-specific carbonate film that is grown uniquely at the interface, where there is direct access to atmospheric CO_2.

The rate of carbonation appears to also be affected by the type of cation. From the PM-IRRAS measurements and the kinetics analysis, the rate of carbonation follows the order of $Ca^{2+} > Mg^{2+} > Na^+ > K^+ > Fe^{2+}$ on high purity iron surfaces. These results are also supported by the fact that alkali and alkaline cations, have been used as promoters on other surfaces for higher CO_2 adsorption.[27 78 79] Bare (metallic) iron surfaces are known to undergo facile CO_2 adsorption,[69 70 71] where the binding of CO_2 on Fe surfaces is strong[80] compared to other catalytic metals, driven by the Lewis basicity and the surface catalytic activity.[78, 81] Potassium promoted Fe(110) have been shown to stabilize surface carbonate, with a dependence of K coverage and the stability of CO_2 adsorbed species.[28] This was also observed for other alkali cations[28], such as Cs promoted Cu(110) and for K promoted Rh.[28] In our studies, the Ca and Mg ions have the higher rate of carbonation, which have been shown to be the highest carbonate forming alkali metals.[23, 27, 32, 58] Here, specific cations at the electrolyte/iron interface may have a promotional effect on adsorption of CO_2 and conversion to surface adsorbed carbonates.

Thirdly, there is a competition between Fe^{2+} and other cations at the interface for growing cation specific carbonate films. During the surface corrosion, the Cl^- pit the surface causing dissolution of Fe^{2+} from the surface into solution, thus initiating reduction-oxidation, as shown in the AFM results. At the interface, the $MgCl_2(aq)$ and $KCl(aq)$ electrolytes enable the formation of carbonate films as opposed to metal hydroxides, suggesting that the Mg^+ and K^+ have either a greater concentration or binding preference for CO_2 in the film growth, thus outcompeting the dissolved Fe^{2+} that could redeposit on the iron surface.[72] When the iron surface was exposed to $FeCl_2(aq)$, the Fe^{2+} quickly corrodes and hydroxylates the surface (shown from the high rate in Figure 3C). Surface carbonates are then grown initially during stage 2, when atmospheric CO_2 and O_2 are adsorbed to the interface. After oxidation in air, γ-FeOOH is formed, replacing the surface carbonates, as shown in Figure 2C and Figure 4. At the region submerged in solution in Fig 4, there is dissolved bicarbonate and oxygen, but no direct exposure to CO_2. Here, the Fe^{2+} cation out competes the K^+ and Mg^{2+} cations for mineral growth, thus producing the same heterogeneous mixture of γ-FeOOH and Fe hydroxy carbonates ($Fe_x(OH)_2CO_3$)).

These results show that cations in electrolytes highly influence mineral carbonation on iron interfaces in complex media, from the direct CO_2 adsorption into the electrolyte. Additionally, surface corrosion, which creates nucleation sites on iron for CO_2 adsorption, is connected with film growth. The findings reveal the synergistic effect of cations from electrolytes, with earth abundant (iron) interfaces at liquid/solid interfaces that could be tailored for direct CO_2 capture for geological sequestration. These studies suggest that reactions at complex interfaces have implications for geochemical mechanisms in planetary environments as well as fundamental processes in surface catalysis and corrosion.

4.0 Conclusions

A surface chemistry approach was used to study the effect of cations on CO_2 capture and interfacial mineral formation and its connection with Fe corrosion at air/solution/Fe interface. The composition and rate of carbonate film formation were found to depend on the cation of the electrolyte. The rate of surface hydroxylation of Fe followed the trend of $Na^+ > K^+ > Fe^{2+}$, which provides basic sites for CO_2 adsorption. Upon exposure to atmospheric CO_2 and O_2 directly from air, the rate of carbonation of iron interfaces was found to follow the order of $Ca^{2+} > Mg^{2+} > Na^+ > K^+ > Fe^{2+}$. The relative elemental composition showed the high concentration of surface carbonate, cations, and chloride at the interface region further confirming the specific cation effect.

At the air/$MgCl_2$(aq)/Fe interface, a film consisting of a mixture of magnesium carbonate, hydromagnesite, and a magnesium iron carbonate hydroxide film. The mineral scale formed at the air/KCl(aq)/Fe interface was found to comprise of a potassium-rich bicarbonate film. For iron in $FeCl_2$(aq), a heterogeneous mixture of γ-FeOOH and iron hydroxy carbonates were produced as the main surface species. These results suggest that direct CO_2 capture occurs from the synergistic effect of nucleation sites, created by surface corrosion, and a promotional effect of cations to grow carbonate films at the air/electrolyte/iron interface.

The rate of iron surface corrosion was measured by the surface roughness using *in situ* AFM analysis. Iron in $MgCl_2$(aq) has a faster initial corrosion rate than Fe in KCl(aq), due to the relative amount of chloride ions. After oxidation in air, the surface corrosion continues in KCl(aq), but plateaus in $MgCl_2$(aq). AFM imaging confirmed the presence of γ-FeOOH and surface hydroxy carbonates in the submerged region, with limited CO_2 exposure, suggesting no direct cation effect. The findings of this study are relevant for developing solutions for direct CO_2 capture and geological sequestration technologies. The details of these surface chemical mechanisms also explain processes at complex interfaces relevant for geochemical formations on Earth and other planets.

Supporting Information Description

The Supporting Information is available free of charge at

List of contents: Example uncorrected PM-IRRAS spectra; Trace metals in iron materials; All PM-IRRAS coverage profiles; Kinetic rates for low-purity Fe samples; natural mineral specimen locality; ATR-FTIR spectra Mg minerals specimens; Table of vibrational assignments; ATR-FTIR spectra of film growth on different regions of the Fe surface; ATR-FTIR spectra of liquid solutions; XPS spectra of the Mg 1s and 2p regions, the Fe 2p region, and the Cl 2p region; AFM images and photographs.

Author contributions

CdA performed the PM-IRRAS and ATR-FTIR experiments and analyzed the PM-IRRAS, ATR-FTIR and XPS data. CdA and KAP wrote the manuscript. KAP edited the final manuscript. KW conducted the AFM corrosion experiments and analysis. KAP perceived the original research idea, designed the experiments, and conceptualized the project. All authors agree with the data presented.

Conflicts of interest

There are no conflicts of interest to declare.

Acknowledgements

This work was supported by National Aeronautics and Space Administration (NASA), under award number NNX15AJ20H through Michigan Space Grant Consortium (MSGC). A part of this study was completed at Michigan Technological University's Applied Chemical and Morphological Analysis Laboratory (ACMAL). We acknowledge National Science Foundation for provide funding for the AFM instrument under MRI CHE1725818.

We would like to acknowledge Dr. Timothy R. Leftwich for his support in collecting XPS data and Daniel Seguin for helping with iron sample polishing. We also thank Alex Marcyan for initially collecting select AFM images. Danica Lemmons and Ryan Mackie are acknowledged for analyzing the data from the $FeCl_2$ and $KHCO_3$ experiments, respectively. We extend our gratitude to the A.E. Seaman Mineral Museum for donating the majority of the natural mineral specimens. Dr. Travis Olds is acknowledged for providing artinite (Cedar Hill Quarry, PA, CM20830) and nesquehonite (Nesquehoning, Carbon County, PA, #1623) from the Carnegie Museum of Natural History collection. The Pokrovskite specimen (Hunting Hill Quarry, Montgomery Co., Maryland, USA, MGMH#142816) was provided courtesy of the Mineralogical & Geological Museum at Harvard University @ copyright 2012, President and Fellows of Harvard College. All rights reserved. This document is based on the Author's version of their PhD thesis, Adambarage Chathura de Alwis, (2022) *Interfacial Oxidation Reactions and Film Nucleation on Iron Surfaces in Complex Environments Using Spectroscopy at the Liquid/Solid and Gas/Solid Interface*, PhD thesis, Michigan Technological University DOI: 10.37099/mtu.dc.etdr/1440.

Present addresses: 1 CA: Intel Corporation, Hillsboro, Oregon, 97124, United States.

2 KW: Clemson University, Department of Chemistry, Clemson, South Carolina 29634, United States

References

(1) Keeling, C. D.; Whorf, T. P. *Atmospheric CO2 records from sites in the SIO air sampling network. In Trends, A Compendium of Data on Global Change.* ; Carbon Dioxide Information Analysis Center, Oak Ridge National Laboratory, U.S. Department of Energy Oak Ridge, TN, U.S.A., 2021, accessed Jan. 2, 2023. https://gml.noaa.gov/ccgg/trends/mlo.html.

(2) Ibrahim, M. H.; El-Naas, M. H.; Benamor, A.; Al-Sobhi, S. S.; Zhang, Z. E. Carbon Mineralization by Reaction with Steel-Making Waste: A Review. *Processes* **2019**, *7* (2), 115. DOI: 10.3390/pr7020115.

(3) Arif, M.; Barifcani, A.; Iglauer, S. Solid/CO2 and solid/water interfacial tensions as a function of pressure, temperature, salinity and mineral type: Implications for CO2-wettability and CO2 geo-storage. *International Journal of Greenhouse Gas Control* **2016**, *53*, 263-273. DOI: 10.1016/j.ijggc.2016.08.020.

(4) Song, C. Global challenges and strategies for control, conversion and utilization of CO2 for sustainable development involving energy, catalysis, adsorption and chemical processing. *Catalysis Today* **2006**, *115* (1-4), 2-32. DOI: 10.1016/j.cattod.2006.02.029.

(5) Kelemen, P. B.; McQueen, N.; Wilcox, J.; Renforth, P.; Dipple, G.; Vankeuren, A. P. Engineered carbon mineralization in ultramafic rocks for CO2 removal from air: Review and new insights. *Chemical Geology* **2020**, *550,* 119628. DOI: 10.1016/j.chemgeo.2020.119628.

(6) Sanna, A.; Uibu, M.; Caramanna, G.; Kuusik, R.; Maroto-Valer, M. M. A review of mineral carbonation technologies to sequester CO2. *Chemical Society Reviews* **2014**, *43* (23), 8049-8080. DOI: 10.1039/c4cs00035h.

(7) Baena-Moreno, F. M.; Rodriguez-Galan, M.; Vega, F.; Alonso-Farinas, B.; Arenas, L. F. V.; Navarrete, B. Carbon capture and utilization technologies: a literature review and recent advances. *Energy Sources Part a-Recovery Utilization and Environmental Effects* **2019**, *41* (12), 1403-1433. DOI: 10.1080/15567036.2018.1548518.

(8) Wang, X. X.; Song, C. S. Carbon Capture From Flue Gas and the Atmosphere: A Perspective. *Frontiers in Energy Research* **2020**, *8*: 560849 DOI: 10.3389/fenrg.2020.560849.

(9) Rampe, E. B.; Bristow, T. F.; Morris, R. V.; Morrison, S. M.; Achilles, C. N.; Ming, D. W.; Vaniman, D. T.; Blake, D. F.; Tu, V. M.; Chipera, S. J.; et al. Mineralogy of Vera Rubin Ridge From the Mars Science Laboratory CheMin Instrument. *Journal of Geophysical Research-Planets* **2020**, *125* (9), e2019JE006306. DOI: 10.1029/2019je006306.

(10) Peretyazhko, T. S.; Ming, D. W.; Morris, R. V.; Agresti, D. G.; Buckley, W. P. Formation of Fe(III) (Hydr)oxides from Fe(II) Sulfides: Implications for Akaganeite Detection on Mars. *ACS Earth and Space Chemistry* **2021**, *5* (8), 1934-1947. DOI: 10.1021/acsearthspacechem.1c00075.

(11) Nie, W.; Ding, A. J.; Wang, T.; Kerminen, V. M.; George, C.; Xue, L. K.; Wang, W. X.; Zhang, Q. Z.; Petaja, T.; Qi, X. M.; et al. Polluted dust promotes new particle formation and growth. *Scientific Reports* **2014**, *4,* 6634. DOI: 10.1038/srep06634.

(12) Rubasinghege, G.; Elzey, S.; Baltrusaitis, J.; Jayaweera, P. M.; Grassian, V. H. Reactions on Atmospheric Dust Particles: Surface Photochemistry and Size-Dependent Nanoscale Redox Chemistry. *Journal of Physical Chemistry Letters* **2010**, *1* (11), 1729-1737. DOI: 10.1021/jz100371d.

(13) Cwiertny, D. M.; Baltrusaitis, J.; Hunter, G. J.; Laskin, A.; Scherer, M. M.; Grassian, V. H. Characterization and acid-mobilization study of iron-containing mineral dust source materials. *Journal of Geophysical Research-Atmospheres* **2008**, *113,* D05202. DOI: 10.1029/2007jd009332.

(14) Voelz, J. L.; Johnson, N. W.; Chun, C. L.; Arnold, W. A.; Penn, R. L. Quantitative Dissolution of Environmentally Accessible Iron Residing in Iron-Rich Minerals: A Review. *Acs Earth and Space Chemistry* **2019**, *3* (8), 1371-1392. DOI: 10.1021/acsearthspacechem.9b00012.

(15) Krasnopolsky, V. A. Variations of the HDO/H2O ratio in the martian atmosphere and loss of water from Mars. *Icarus* **2015**, *257*, 377-386. DOI: 10.1016/j.icarus.2015.05.021.

(16) Vaniman, D. T.; Bish, D. L.; Ming, D. W.; Bristow, T. F.; Morris, R. V.; Blake, D. F.; Chipera, S. J.; Morrison, S. M.; Treiman, A. H.; Rampe, E. B.; et al. Mineralogy of a Mudstone at

Yellowknife Bay, Gale Crater, Mars. *Science* **2014**, *343,* 1243480. DOI: 10.1126/science.1243480.

(17) Ming, D. W.; Gellert, R.; Morris, R. V.; Arvidson, R. E.; Brukner, J.; Clark, B. C.; Cohen, B. A.; d'Uston, C.; Economou, T.; Fleischer, I.; et al. Geochemical properties of rocks and soils in Gusev Crater, Mars: Results of the Alpha Particle X-Ray Spectrometer from Cumberland Ridge to Home Plate. *Journal of Geophysical Research-Planets* **2008**, *113,* E12S39. DOI: 10.1029/2008je003195.

(18) Lyu, Y. L.; Qu, Z. Q.; Liu, L. Y.; Guo, L. L.; Yang, Y. Y.; Hu, X.; Xiong, Y. Y.; Zhang, G. M.; Zhao, M. D.; Liang, B.; et al. Characterization of dustfall in rural and urban sites during three dust storms in northern China, 2010. *Aeolian Research* **2017**, *28*, 29-37. DOI: 10.1016/j.aeolia.2017.06.004.

(19) Sarin, P.; Snoeyink, V. L.; Bebee, J.; Jim, K. K.; Beckett, M. A.; Kriven, W. M.; Clement, J. A. Iron release from corroded iron pipes in drinking water distribution systems: effect of dissolved oxygen. *Water Research* **2004**, *38* (5), 1259-1269. DOI: 10.1016/j.watres.2003.11.022.

(20) Cha, S. C.; Spiegel, M. Local reactions of KCl particles with iron, nickel and chromium surfaces. *Materials and Corrosion-Werkstoffe Und Korrosion* **2006**, *57* (2), 159-164. DOI: 10.1002/maco.200503903.

(21) Tosca, N. J.; McLennan, S. M.; Dyar, M. D.; Sklute, E. C.; Michel, F. M. Fe oxidation processes at Meridiani Planum and implications for secondary Fe mineralogy on Mars. *Journal of Geophysical Research-Planets* **2008**, *113,* E05005. DOI: 10.1029/2007je003019.

(22) Huang, J. Z.; Jones, A.; Waite, T. D.; Chen, Y. L.; Huang, X. P.; Rosso, K. M.; Kappler, A.; Mansor, M.; Tratnyek, P. G.; Zhang, H. C. Fe(II) Redox Chemistry in the Environment. *Chemical Reviews* **2021**, *121* (13), 8161-8233. DOI: 10.1021/acs.chemrev.0c01286.

(23) Qomi, M. J. A.; Miller, Q. R. S.; Zare, S.; Schaef, H. T.; Kaszuba, J. P.; Rosso, K. M. Molecular-scale mechanisms of CO2 mineralization in nanoscale interfacial water films. *Nature Reviews Chemistry* **2022**, *6* (9), 598-613. DOI: 10.1038/s41570-022-00418-1.

(24) Snaebjornsdottir, S. O.; Sigfusson, B.; Marieni, C.; Goldberg, D.; Gislason, S. R.; Oelkers, E. H. Carbon dioxide storage through mineral carbonation. *Nature Reviews Earth & Environment* **2020**, *1* (2), 90-102. DOI: 10.1038/s43017-019-0011-8.

(25) Boyd, C. E. *Water Quality, An Introduction* Springer Nature, 2020.

(26) Ostovari, H.; Muller, L.; Skocek, J.; Bardow, A. From Unavoidable CO2 Source to CO2 Sink? A Cement Industry Based on CO2 Mineralization. *Environmental Science & Technology* **2021**, *55* (8), 5212-5223. DOI: 10.1021/acs.est.0c07599.

(27) Omodolor, I. S.; Otor, H. O.; Andonegui, J. A.; Allen, B. J.; Alba-Rubio, A. C. Dual-Function Materials for CO2 Capture and Conversion: A Review. *Industrial & Engineering Chemistry Research* **2020**, *59* (40), 17612-17631. DOI: 10.1021/acs.iecr.0c02218.

(28) Freund, H. J.; Roberts, M. W. Surface chemistry of carbon dioxide. *Surface Science Reports* **1996**, *25* (8), 225-273. DOI: 10.1016/s0167-5729(96)00007-6.

(29) Zhu, C.; Wang, H.; Li, G.; An, S. Y.; Ding, X. F.; Teng, H. H.; Zhao, L. CO2 Absorption and Magnesium Carbonate Precipitation in MgCl2-NH3-NH4Cl Solutions: Implications for Carbon Capture and Storage. *Minerals* **2017**, *7* (9) 172. DOI: 10.3390/min7090172.

(30) Couling, D. J.; Das, U.; Green, W. H. Analysis of Hydroxide Sorbents for CO2 Capture from Warm Syngas. *Industrial & Engineering Chemistry Research* **2012**, *51* (41), 13473-13481. DOI: 10.1021/ie300189a.

(31) Mirabella, F.; Zaki, E.; Ivars-Barcelo, F.; Schauermann, S.; Shaikhutdinov, S.; Freund, H. J. CO2 Adsorption on Magnetite Fe3O4(111). *Journal of Physical Chemistry C* **2018**, *122* (48), 27433-27441. DOI: 10.1021/acs.jpcc.8b08240.

(32) Sanz-Perez, E. S.; Murdock, C. R.; Didas, S. A.; Jones, C. W. Direct Capture of CO2 from Ambient Air. *Chemical Reviews* **2016**, *116* (19), 11840-11876. DOI: 10.1021/acs.chemrev.6b00173.

(33) de Alwis, C.; Trought, M.; Lundeen, J.; Perrine, K. A. Effect of Cations on the Oxidation and Atmospheric Corrosion of Iron Interfaces to Minerals. *Journal of Physical Chemistry A* **2021**, *125* (36), 8047-8063. DOI: 10.1021/acs.jpca.1c06451.

(34) de Alwis, C.; Leftwich, T. R.; Perrine, K. A. New Approach to Simultaneous In Situ Measurements of the Air/Liquid/Solid Interface Using PM-IRRAS. *Langmuir* **2020**, *36* (13), 3404-3414. DOI: 10.1021/acs.langmuir.9b03958.

(35) de Alwis, C.; Perrine, K. A. In Situ PM-IRRAS at the Air/Electrolyte/Solid Interface Reveals Oxidation of Iron to Distinct Minerals. *Journal of Physical Chemistry A* **2020**, *124* (33), 6735-6744. DOI: 10.1021/acs.jpca.0c03592.

(36) Seah, M. P.; Gilmore, I. S. Quantitative x-ray photoelectron spectroscopy: Quadrupole effects, shake-up, Shirley background, and relative sensitivity factors from a database of true x-ray photoelectron spectra. *Physical Review B* **2006**, *73* (17), 174113. DOI: 10.1103/PhysRevB.73.174113.

(37) Seah, M. P.; Gilmore, I. S.; Spencer, S. J. Quantitative XPS I. Analysis of X-ray photoelectron intensities from elemental data in a digital photoelectron database. *Journal of Electron Spectroscopy and Related Phenomena* **2001**, *120* (1-3), 93-111. DOI: 10.1016/s0368-2048(01)00311-5.

(38) Baltrusaitis, J.; Schuttlefield, J.; Zeitler, E.; Grassian, V. H. Carbon dioxide adsorption on oxide nanoparticle surfaces. *Chemical Engineering Journal* **2011**, *170* (2-3), 471-481. DOI: 10.1016/j.cej.2010.12.041.

(39) Philipp, R.; Fujimoto, K. FTIR SPECTROSCOPIC STUDY OF CO2 ADSORPTION/DESORPTION ON MGO/CAO CATALYSTS. *Journal of Physical Chemistry* **1992**, *96* (22), 9035-9038. DOI: 10.1021/j100201a063.

(40) Harms, L.; Brand, I. Application of PM IRRAS to study structural changes of the magnesium surface in corrosive environments. *Vibrational Spectroscopy* **2018**, *97*, 106-113. DOI: 10.1016/j.vibspec.2018.06.006.

(41) White, W. B. Infrared Characterization of Water and Hydroxyl Ion in the Basic Magnesium Carbonate Minerals. *The American Mineralogist* **1971**, *56*, 46-53.

(42) Frost, R. L.; Palmer, S. J. Infrared and infrared emission spectroscopy of nesquehonite Mg(OH)(HCO3)center dot 2H(2)O-implications for the formula of nesquehonite. *Spectrochimica Acta Part A-Molecular and Biomolecular Spectroscopy* **2011**, *78* (4), 1255-1260. DOI: 10.1016/j.saa.2010.12.059.

(43) Botha, A.; Strydom, C. A. DTA and FT-IR analysis of the rehydration of basic magnesium carbonate. *Journal of Thermal Analysis and Calorimetry* **2003**, *71* (3), 987-995. DOI: 10.1023/a:1023355016208.

(44) Gao, W. L.; Zhou, T. T.; Wang, Q. Controlled synthesis of MgO with diverse basic sites and its CO2 capture mechanism under different adsorption conditions. *Chemical Engineering Journal* **2018**, *336*, 710-720. DOI: 10.1016/j.cej.2017.12.025.

(45) Hausner, D. B.; Bhandari, N.; Pierre-Louis, A. M.; Kubicki, J. D.; Strongin, D. R. Ferrihydrite reactivity toward carbon dioxide. *Journal of Colloid and Interface Science* **2009**, *337* (2), 492-500. DOI: 10.1016/j.jcis.2009.05.069.

(46) Baltrusaitis, J.; Jensen, J. H.; Grassian, V. H. FTIR Spectroscopy combined with isotope labeling and quantum chemical calculations to investigate adsorbed bicarbonate formation following reaction of carbon dioxide with surface hydroxyl groups on Fe(2)O3 and Al2O3. *Journal of Physical Chemistry B* **2006**, *110* (24), 12005-12016. DOI: 10.1021/jp057437j.

(47) Baltrusaitis, J.; Grassian, V. H. Surface reactions of carbon dioxide at the adsorbed water-iron oxide interface. *Journal of Physical Chemistry B* **2005**, *109* (25), 12227-12230. DOI: 10.1021/jp051868k.

(48) Farmer, V. C. *Vibrational Spectroscopy in Mineral Chemistry*; Mineralogical Society, 1974. DOI: 10.1180/mono-4.1.

(49) Hiremath, V.; Kwon, H. J.; Jung, I. S.; Kwon, S.; Kwon, S. H.; Lee, S. G.; Lee, H. C.; Seo, J. G. Mg-Ion Inversion in MgO@MgO-Al2O3 Oxides: The Origin of Basic Sites. *Chemsuschem* **2019**, *12* (12), 2810-2818. DOI: 10.1002/cssc.201900072.

(50) McCutcheon, J.; Power, I. M.; Shuster, J.; Harrison, A. L.; Dipple, G. M.; Southam, G. Carbon Sequestration in Biogenic Magnesite and Other Magnesium Carbonate Minerals. *Environmental Science & Technology* **2019**, *53* (6), 3225-3237. DOI: 10.1021/acs.est.8b07055.

(51) McCafferty, E. *Introduction to Corrosion Science*; Springer, 2010.

(52) Song, Y. R.; Jiang, G. M.; Chen, Y.; Zhao, P.; Tian, Y. M. Effects of chloride ions on corrosion of ductile iron and carbon steel in soil environments. *Scientific Reports* **2017**, *7*, 6865. DOI: 10.1038/s41598-017-07245-1.

(53) Soulie, V.; Lequien, F.; Ferreira-Gomes, F.; Moine, G.; Feron, D.; Prene, P.; Moehwald, H.; Zemb, T.; Riegler, H. Salt-induced iron corrosion under evaporating sessile droplets of aqueous sodium chloride solutions. *Materials and Corrosion-Werkstoffe Und Korrosion* **2017**, *68* (9), 927-934. DOI: 10.1002/maco.201609319.

(54) Lanas, J.; Alvarez, J. I. Dolomitic lime: thermal decomposition of nesquehonite. *Thermochimica Acta* **2004**, *421* (1-2), 123-132. DOI: 10.1016/j.tca.2004.04.007.

(55) Lewis, D. G.; Farmer, V. C. Infrared -Absorption of Surface Hydroxyl Groups and Lattice Vibrations in Lepidocrocite (Gamma-FeOOH) and Boehmite (Gamma-AlOOH). *Clay Minerals* **1986**, *21* (1), 93-100. DOI: 10.1180/claymin.1986.021.1.08.

(56) Roychowdhury, T.; Bahr, S.; Dietrich, P.; Meyer, M.; Thissen, A.; Linford, M. R. Calcite (CaCO3), by near-ambient pressure XPS. *Surface Science Spectra* **2019**, *26* (1) 014025. DOI: 10.1116/1.5109266.

(57) Stoch, J.; Gablankowskakukucz, J. THE EFFECT OF CARBONATE CONTAMINATIONS ON THE XPS-O-1S BAND-STRUCTURE IN METAL-OXIDES. *Surface and Interface Analysis* **1991**, *17* (3), 165-167. DOI: 10.1002/sia.740170308.

(58) Tao, L.; Huang, J. C.; Dastan, D.; Wang, T. Y.; Li, J.; Yin, X. T.; Wang, Q. New insight into absorption characteristics of CO2 on the surface of calcite, dolomite, and magnesite. *Applied Surface Science* **2021**, *540*, 148320. DOI: 10.1016/j.apsusc.2020.148320.

(59) Pettersson, J.; Folkeson, N.; Johansson, L. G.; Svensson, J. E. The Effects of KCl, K2SO4 and K2CO3 on the High Temperature Corrosion of a 304-Type Austenitic Stainless Steel. *Oxidation of Metals* **2011**, *76* (1-2), 93-109. DOI: 10.1007/s11085-011-9240-z.

(60) Karlsson, S.; Larsson, E.; Jonsson, T.; Svensson, J. E.; Liske, J. A Laboratory Study of the in Situ Sulfation of Alkali Chloride Rich Deposits: Corrosion Perspective. *Energy & Fuels* **2016**, *30* (9), 7256-7267. DOI: 10.1021/acs.energyfuels.6b00372.

(61) Mansoori, H.; Young, D.; Brown, B.; Singer, M. Influence of calcium and magnesium ions on CO₂ corrosion of carbon steel in oil and gas production systems - A review. *Journal of Natural Gas Science and Engineering* **2018**, *59*, 287-296. DOI: 10.1016/j.jngse.2018.08.025.

(62) Liu, A. R.; Liu, J.; Pan, B. C.; Zhang, W. X. Formation of lepidocrocite (gamma-FeOOH) from oxidation of nanoscale zero-valent iron (nZVI) in oxygenated water. *RSC Advances* **2014**, *4* (101), 57377-57382. DOI: 10.1039/c4ra08988j.

(63) Antony, H.; Legrand, L.; Chausse, A. Carbonate and sulphate green rusts - Mechanisms of oxidation and reduction. *Electrochimica Acta* **2008**, *53* (24), 7146-7156. DOI: 10.1016/j.electacta.2008.05.008.

(64) Legrand, L.; Abdelmoula, M.; Gehin, A.; Chausse, A.; Genin, J. M. R. Electrochemical formation of a new Fe(II)-Fe(III) hydroxy-carbonate green rust: characterisation and morphology. *Electrochimica Acta* **2001**, *46* (12), 1815-1822. DOI: 10.1016/s0013-4686(00)00728-3.

(65) Frankel, G. S.; Li, T. S.; Scully, J. R. Localized Corrosion: Passive Film Breakdown vs Pit Growth Stability. *Journal of the Electrochemical Society* **2017**, *164* (4), C180-C181. DOI: 10.1149/2.1381704jes.

(66) Adhikari, N. M.; Tuladhar, A.; Wang, Z. M.; De Yoreo, J. J.; Rosso, K. M. No Hydrogen Bonding between Water and Hydrophilic Single Crystal MgO Surfaces? *Journal of Physical Chemistry C* **2021**, *125* (47), 26132-26138. DOI: 10.1021/acs.jpcc.1c06486.

(67) Mutch, G. A.; Anderson, J. A.; Vega-Maza, D. Surface and bulk carbonate formation in calcium oxide during CO2 capture. *Applied Energy* **2017**, *202*, 365-376. DOI: 10.1016/j.apenergy.2017.05.130.

(68) Mutch, G. A.; Shulda, S.; McCue, A. J.; Menart, M. J.; Ciobanu, C. V.; Ngo, C.; Anderson, J. A.; Richards, R. M.; Vega-Maza, D. Carbon Capture by Metal Oxides: Unleashing the Potential of the (111) Facet. *Journal of the American Chemical Society* **2018**, *140* (13), 4736-4742. DOI: 10.1021/jacs.8b01845.

(69) Wang, H. Z.; Nie, X. W.; Chen, Y. G.; Guo, X. W.; Song, C. S. Facet effect on CO2 adsorption, dissociation and hydrogenation over Fe catalysts: Insight from DFT. *Journal of CO2 Utilization* **2018**, *26*, 160-170. DOI: 10.1016/j.jcou.2018.05.003.

(70) Glezakou, V. A.; Dang, L. X. Spontaneous Activation of CO2 and Possible Corrosion Pathways on the Low-Index Iron Surface Fe(100). *Journal of Physical Chemistry C* **2009**, *113* (9), 3691-3696. DOI: 10.1021/jp808296c.

(71) Notini, L.; Latta, D. E.; Neumann, A.; Pearce, C. I.; Sassi, M.; N'Diaye, A. T.; Rosso, K. M.; Scherer, M. M. The Role of Defects in Fe(II)-Goethite Electron Transfer. *Environmental Science & Technology* **2018**, *52* (5), 2751-2759. DOI: 10.1021/acs.est.7b05772.

(72) de Vasquez, M. G. V.; Rudd, B. A. W.; Baer, M. D.; Beasley, E. E.; Allen, H. C. Role of Hydration in Magnesium versus Calcium Ion Pairing with Carboxylate: Solution and the Aqueous Interface. *Journal of Physical Chemistry B* **2021**, *125* (40), 11308-11319. DOI: 10.1021/acs.jpcb.1c06108.

(73) Callahan, K. M.; Casillas-Ituarte, N. N.; Xu, M.; Roeselova, M.; Allen, H. C.; Tobias, D. J. Effect of Magnesium Cation on the Interfacial Properties of Aqueous Salt Solutions. *Journal of Physical Chemistry A* **2010**, *114* (32), 8359-8368. DOI: 10.1021/jp103485t.

(74) Denton, J. K.; Kelleher, P. J.; Johnson, M. A.; Baer, M. D.; Kathmann, S. M.; Mundy, C. J.; Rudd, B. A. W.; Allen, H. C.; Choi, T. H.; Jordan, K. D. Molecular-level origin of the carboxylate head group response to divalent metal ion complexation at the air-water interface. *Proceedings of*

the National Academy of Sciences of the United States of America **2019**, *116* (30), 14874-14880. DOI: 10.1073/pnas.1818600116.

(75) Kraushofer, F.; Mirabella, F.; Xu, J.; Pavelec, J.; Balajka, J.; Mullner, M.; Resch, N.; Jakub, Z.; Hulva, J.; Meier, M.; et al. Self-limited growth of an oxyhydroxide phase at the Fe3O4(001) surface in liquid and ambient pressure water. *Journal of Chemical Physics* **2019**, *151* (15), 154702. DOI: 10.1063/1.5116652.

(76) Baltrusaitis, J.; Schuttlefield, J. D.; Zeitler, E.; Jensen, J. H.; Grassian, V. H. Surface reactions of carbon dioxide at the adsorbed water-oxide interface. *Journal of Physical Chemistry C* **2007**, *111* (40), 14870-14880. DOI: 10.1021/jp074677l.

(77) Miller, Q. R. S.; Dixon, D. A.; Burton, S. D.; Walter, E. D.; Hoyt, D. W.; McNeill, A. S.; Moon, J. D.; Thanthiriwatte, K. S.; Ilton, E. S.; Qafoku, O.; et al. Surface-Catalyzed Oxygen Exchange during Mineral Carbonation in Nanoscale Water Films. *Journal of Physical Chemistry C* **2019**, *123* (20), 12871-12885. DOI: 10.1021/acs.jpcc.9b02215.

(78) Wang, S. G.; Liao, X. Y.; Cao, D. B.; Huo, C. F.; Li, Y. W.; Wang, J. G.; Jiao, H. J. Factors controlling the interaction of CO2 with transition metal surfaces. *Journal of Physical Chemistry C* **2007**, *111* (45), 16934-16940. DOI: 10.1021/jp074570y.

(79) Mendoza, E. Y. M.; Santos, A. S.; Lopez, E. V.; Drozd, V.; Durygin, A.; Chen, J. H.; Saxena, S. K. Iron oxides as efficient sorbents for CO2 capture. *Journal of Materials Research and Technology* **2019**, *8* (3), 2944-2956. DOI: 10.1016/j.jmrt.2019.05.002.

(80) Li, X.; Paier, J. Adsorption of Water on the Fe3O4(111) Surface: Structures, Stabilities, and Vibrational Properties Studied by Density Functional Theory. *Journal of Physical Chemistry C* **2016**, *120* (2), 1056-1065. DOI: 10.1021/acs.jpcc.5b10560.

(81) Jun, Y. S.; Zhang, L. J.; Min, Y. J.; Li, Q. Y. Nanoscale Chemical Processes Affecting Storage Capacities and Seals during Geologic CO2 Sequestration. *Accounts of Chemical Research* **2017**, *50* (7), 1521-1529. DOI: 10.1021/acs.accounts.6b00654.

TOC Graphic